Tribology International 190 (2023) 109063

Contents lists available at ScienceDirect

Tribology International

journal homepage: www.elsevier.com/locate/triboint

Microstructural, mechanical, tribological, and corrosion behavior of ultrafine bio-degradable Mg/CeO_2 nanocomposites: Machine learning-based modeling and experiment

Surja Deka [a], Farzin Mozafari [b], Ashis Mallick [a,*]

[a] Department of Mechanical Engineering, Indian Institute of Technology (ISM) Dhanbad, Jharkhand, India
[b] Department of Mechanical Engineering, Abdullah Gül University, Kayseri, Turkey

ARTICLE INFO

Keywords:
Microstructural characterization
Tribological properties
Corrosion
Machine learning

ABSTRACT

The present study investigated the microstructural, mechanical, tribological, and corrosion behavior of near-dense and low-volume fraction magnesium-cerium dioxide (Mg/CeO_2) (x = 0.5, 1, and 1.5 vol.%) nanocomposites synthesized by in-situ hot extrusion assisted powder metallurgy (PM) process. Results showed a significant improvement in wear resistance for Mg/CeO_2 nanocomposite compared to monolithic Mg at varied applied loads. Microindentation tests were performed to access the Vickers microhardness homogeneity along the extrusion direction. The corrosion analysis revealed that introducing ceria nanoparticles enhanced Mg's corrosion resistance and expedited the development of an apatite layer on the surface, providing enhanced protection. A feedforward neural network and Long Short-Term Memory (LSTM) network were also developed to characterize nanocomposites' wear and corrosion behavior.

1. Introduction

The need for novel metal-based biomaterials for artificial implants has been steadily increasing. It is projected to grow further to meet the needs of people suffering from bone injuries and deterioration caused by accidents, sports injuries, or the natural aging process, which frequently necessitate biomaterial implants to restore function [1]. Research suggests using conventional metallic biomaterials such as titanium (Ti) and some of its alloys, cobalt-chromium (Co-Cr) alloys, Zinc(Zn)-based alloys, Iron (Fe)-based alloys, and stainless steels (SS) for usage, but they possess greater elastic moduli than natural bone (Ti-based alloys: 100–110 GPa, stainless steels: 190–205 GPa, Zn-based alloys: 90–100 GPa, Fe-based alloys: 200 GPa, natural bone: 10–30 GPa [2]), which triggers the "stress-shielding" phenomenon and can cause post-implantation challenges such as bone resorption and implant loosening [1]. In this context, biodegradable magnesium (Mg) alloys have demonstrated their acceptance for biomedical applications due to their mechanical similarities to bone tissues, closer elastic moduli (40–45 GPa) to that of natural bone (10–30 GPa) [3], more excellent ductility relative to bioceramics [4], exceptional biocompatibility [5], and their capacity to dissolve spontaneously in the bodily environment [6].

In the past few years, Mg and its alloys have been actively researched as prospective degradable materials for diverse applications in bone tissue engineering, orthopedics, and cardiovascular field due to their high specific strength, low weight, and biodegradability [7,8]. In addition, Mg is the fourth most prevalent cation in the body and is involved in about 300 enzymatic activities; therefore, the human metabolism can handle Mg ions generated during breakdown [9]. Despite the promising prospect of pure Mg, it lacks mechanical strength and ductility and releases a substantial amount of hydrogen upon decomposition in the physiological environment prior to adequate bone healing. According to studies, alloying Mg with other alloying elements like aluminum (Al), zinc (Zn), zirconium (Zr), calcium (Ca), manganese (Mn), and certain rare earth elements (REEs) can help Mg overcome the aforementioned issues and achieve the requisite mechanical and corrosion properties. However, due to the release of unwanted corrosion products and metal ions from alloying elements during deterioration, these Mg alloys may exhibit uneven corrosion with significant H_2 evolution. They may produce toxicity and allergy reactions in the physiological environment [2,7,10]. In addition to corrosion issues, it is essential to note that Mg and its alloys are less

* Corresponding author.
E-mail address: mal123_us@yahoo.com (A. Mallick).

https://doi.org/10.1016/j.triboint.2023.109063
Received 10 August 2023; Received in revised form 22 September 2023; Accepted 28 October 2023
Available online 31 October 2023

frequently used in abrasion-prone sensitive parts due to their inadequate wear resistance qualities [11]. Mg-based parts exhibit a reduced lifespan due to wear, making them unsuitable for use in gears, bearings, cylinders, and pistons, which is a major problem in the mechanical profession [12–14].

To address the limitations as mentioned earlier, an alternative to alloying has been proposed wherein various ceramic and metal reinforcing phases like SiC, TiC, TiB_2, ZrO_2, graphene nanoplatelets (GNPs), TiO_2, Al_2O_3, and Mg_2S are added to the Mg to synthesize Mg matrix nanocomposites (Mg MNCs) in order to enhance their mechanical, tribological, corrosion, creep, and chemical properties [11,15,16]. For instance, Turan et al. [17] and Shahin et al. [6] reported that dispersing the nano-sized graphene (GNP) reinforcement in the Mg matrix established a strong chemical interaction between Mg and GNP, which led to a decrease in the wear rate and an increase in the corrosion resistance of Mg MMNCs. For a more in-depth understanding, see the research of Razabi et al. [18] and Kaviti et al. [11].

In comparison to other types of ceramic oxide nanoparticles (NPs), rare-earth oxide (REO) NPs have proven to offer the most beneficial results in terms of minimizing segregation at grain boundaries, increasing the endurance of the microstructure against coarsening, and being used in high-temperature applications, which strongly encourages the development of novel REO-containing Mg-based nanocomposites with superior properties. Among rare-earth oxides, cerium oxide (CeO_2) is a desirable rare-earth oxide reinforcement due to its unique combination of variable valence, high thermal stability, more significant corrosion and wear resistance, superior electronic and optical properties, high elastic modulus, high refractive index, UV absorbing ability, low reduction potential and pore-blocking properties [19–23]. Hence, CeO_2 could be used as reinforcement in Mg to improve the metal's mechanical, corrosion and tribological properties.

To the best of the authors' knowledge, there have been two instances where CeO_2 nanoparticles (CNPs) have been introduced to Mg MMNC to study their characteristics [23,24]. Recently, Kujur and her team [23] examined the influence of CNPs on the microstructural, damping, mechanical, and thermal properties of Mg MMNC. According to the study, the gradual addition of CNPs to the matrix increased hardness. This was due to CeO_2 NPs' ability to slow down dislocation movement and CNPs' ability to prevent the recrystallization and growth of crystal grains. Furthermore, the nanocomposites enhanced the ignition response, damping behavior, and mechanical characteristics of Mg MMNCs. However, the study did not investigate the corrosion and tribological capabilities of the nanocomposites. In a different study, Kujur and colleagues [24] investigated the mechanical and biological properties of CeO_2-reinforced Mg-Zn alloy, exhibiting good mechanical properties and corrosion resistance. However, the strength of the nanocomposites could be improved for usage in corrosive environments, which demand strong mechanical integrity of the material. Also, the study failed to address the tribological capabilities of the Mg MMNCs. Therefore, further research is strongly recommended into the tribological and corrosion capabilities of the Mg/CeO_2 nanocomposites.

In the context of the synthesis of Mg-based nanocomposites, the literature supports a variety of approaches, such as powder metallurgy (PM), casting, hot bonding method, sol–gel technology, spark plasma sintering method, high-pressure coupling with classic sintering, laser melting, and ultrasonic cavitation [15,25]. A potential challenge in producing Mg MMNCs is the difficulty in maintaining a homogeneous distribution of NPs throughout the matrix, particularly for greater volume fractions of reinforcement [26,27]. In this regard, the PM method is considered superior because it allows relatively uniform distribution of the reinforcing phase within the matrix material and also due to the low production temperatures that minimize adverse reactions between the matrix and reinforcing materials.

Artificial intelligence and machine learning have been successfully used to model the properties of materials because they have an advantage over analytical solutions [28]. They do not necessitate the mathematical formulation of the problem, which can be difficult for many materials, especially nanocomposites and alloys. Furthermore, machine learning algorithms can handle issues with high accuracy and minimal computational cost, unlike finite element simulation and molecular dynamics simulation, which have significant computational cost and time requirements [29]. Machine learning is most advantageous for highly nonlinear issues where the response is governed by various material properties, such as alloys and nanocomposites, which call for highly accurate numerical models to forecast their behavior. For instance, recently, Aydin et al. [30] established machine learning algorithms to predict the wear behavior of Mg nanocomposites under different test conditions. The results showed that neural network models produce the best results with the highest level of accuracy in predicting wear properties for nanocomposite. Recently, Kavimania et al. [31] investigated the wear behavior of Mg/SiC-rGO nanocomposite using Taguchi-coupled ANN. The composite's wear rate was estimated using an ANN prediction model with a 5-8-1 network structure. According to their research, the proposed models were 99.8% accurate in predicting different wear factors' effects. Recently, Pagadala et al. [32] predicted the rate of corrosion in Mg alloy exposed to a simulated bodily fluid using an extreme gradient boosting (XGB) machine learning model. The XGB algorithm accurately estimated the corrosion rate in Mg alloy samples that were submerged in SBF for various durations. Chaluvaraju et al. [33] recently employed ANN to estimate the corrosion resistance of an Al_2O_3 reinforced Al-Mg alloy composite by utilizing the response surface method (RSM) technique. The study reported obtaining 99.9% accurate predictions by changing the number of neurons in the hidden layer from 6 to 16. Despite its popularity in recent years, there have been few studies based on the use of machine learning models in understanding the wear and corrosion behavior of Mg MMNC. The literature supports no studies on the tribological and corrosion behavior of rare earth oxide-mediated Mg MMNC in SBF. Therefore, further investigation into these areas is strongly recommended.

The literature review demonstrates that no attempts have been made to synthesize Mg/CeO_2 nanocomposites employing high-energy ball milling assisted in-situ hot extrusion-based PM process. It is also worth noting that the literature contains no studies that have addressed the coupled wear and corrosion analysis of CNP-reinforced ultrafine Mg MMNCs. Therefore, the primary objective of the present study is to develop and systematically investigate how high-energy ball milling and reinforcement content influence the microstructural, mechanical, tribological, and corrosion properties of monolithic Mg and Mg/CeO_2 nanocomposites. Correlations were established between the ultrafine microstructure of the nanocomposites introduced by mechanical alloying and the aforementioned properties to gain insight into the vital significance of refined microstructure. The study's second objective is to develop and evaluate machine-learning approaches for predicting wear and corrosion in nanocomposites. Specifically, one neural network is designed to predict wear rates using applied load and nanoparticle volume fraction, while the other network predicts corrosion rates using immersion time and volume fraction as input features. The aim is to assess the accuracy and effectiveness of these models in capturing the behaviors of wear and corrosion in Mg/CeO_2 nanocomposites.

2. Experimental details

2.1. Materials

In the present study, Mg powder was employed as the matrix material and was procured from Sigma Aldrich (USA). The reinforcing agent was CeO_2, procured from Alfa Aesar Corporation (Ward Hill, MA). Hanks' balanced salt solution (HBSS) was used as a simulated bodily fluid for corrosion testing and was procured from Sigma Aldrich (USA). For more information on the materials' properties, refer to Table 1.

Table 1
The characteristics of matrix (Mg), reinforcing agent (CeO_2) and Hanks' balanced salt solution.

Material	Purity	Particle size (μm)	Density (g/cc)	Company
Mg	≥99	32	1.74	Sigma Aldrich (USA)
CeO_2	≥99.5	0.03	7.132	Alfa Aesar Corporation (Ward Hill, MA)
Hanks Balanced Salt solution	–	–	–	Alfa Aesar Corporation (Ward Hill, MA)
Kontakt Chemie Graphit 33	–	–	–	Kontakt Chemie, Germany

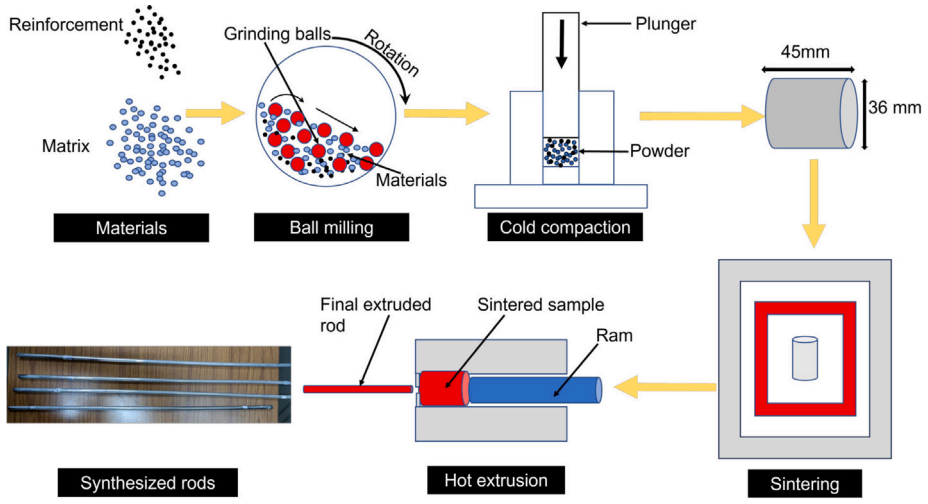

Fig. 1. Schematic illustration of the synthesizing procedure.

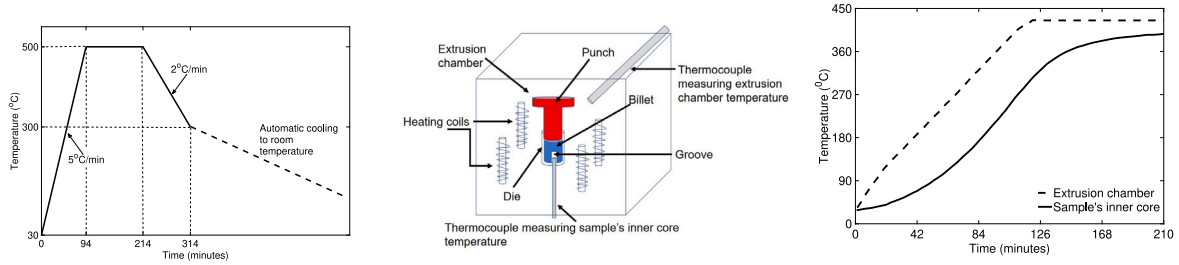

Fig. 2. (a) Schematic illustration of the sintering process, (b) Illustration of the setup used to measure the actual temperature of the sample's inner core and (c) temperature variation of the extrusion chamber and sample's inner core.

2.2. Preparation of the nanocomposites

The ceria-reinforced Mg MMNCs were synthesized using ball milling assisted in-situ hot extrusion-based PM process. The schematic illustration of the synthesizing process is shown in Fig. 1. The first step of the synthesizing process was to efficiently blend the matrix and reinforcement in an attributor mill to obtain a uniform distribution of the reinforcement within the matrix. The high-energy ball milling (HEBM) was carried out at 200 rpm for 5 h (run for 20 min, then rest for 5 min) in stainless steel jars with 16 mm stainless steel balls (316 grade). It is also worth noting that HEBM of nanocomposite powder mixtures resulted in ultrafine powder mixtures due to the reduction of the crystallite size of the powders. During the ball milling process, the ball-to-powder ratio was kept constant at 10:1. Zinc stearate was employed as a process control agent (PCA) at a low concentration of 1.5 wt.% to impede cold welding in powders and prevent agglomeration of reinforcements. Next, the powder mixtures were put into a 36-mm-diameter compaction mold, then cold-pressed under a 50-ton load to make composites (35 in diameter and 45 mm in height). Subsequently, sintering was performed in a tubular furnace at a maximum temperature of 500 °C (~77% of the melting temperature of Mg) in an argon atmosphere. Fig. 2(a) illustrates the particulars of the sintering process. Finally, hot extrusion was carried out in an argon atmosphere at 395 °C with an extrusion ratio of 20.25:1, yielding extruded rods with 8 mm in diameter and 300 mm in length. A graphite spray (Kontakt Chemie Graphit 33) was used as a lubricant to reduce the friction between the inner wall of the extrusion die and the surface of the samples. The details of the extrusion process have been provided in Fig. 2(b) and Fig. 2(c).

2.3. Characterization methods

Microindentation tests were conducted using a Vickers hardness machine (Model: MTR3/50-50/NI instrument, MICROTEST S.A., Spain) with a loading rate of 5 N/min and a dwell period of 30 s. The tests were repeated eight times to ensure that the results were consistent. Microindentation tests were conducted using a Vickers hardness machine (Model: MTR3/50-50/NI instrument, MICROTEST S.A., Spain) with a loading rate of 5 N/min and a dwell period of 30 s. The tests were repeated eight times to ensure that the results were consistent. A reciprocating-type ball-on-plate universal tribometer (MFT 5000, Rtec instruments, USA) was used to investigate the dry sliding wear behavior of Mg/CeO_2 nanocomposites. A stainless steel ball (6 mm diameter) was used as a counter body for the wear tests, and Mg/CeO_2

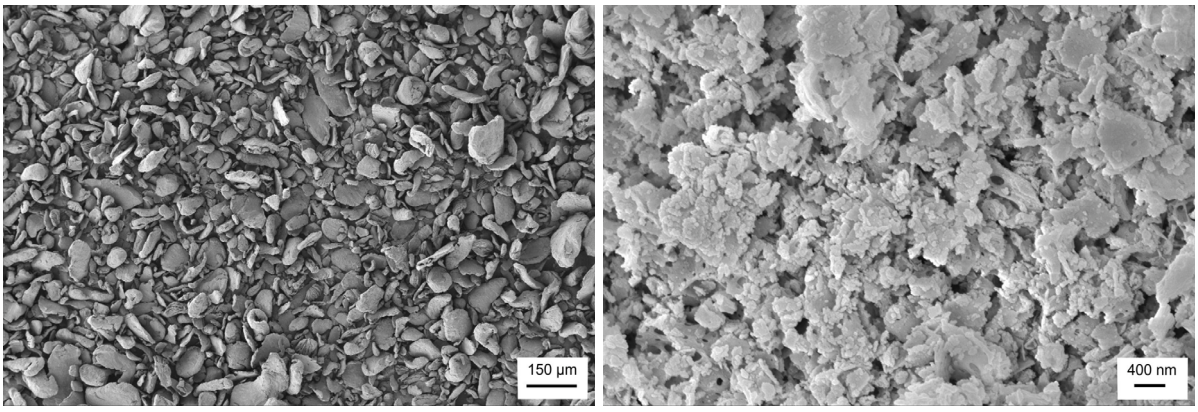

Fig. 3. FESEM micrographs of as-received (a) Mg powder and (b) CeO_2 nanoparticles.

nanocomposites were used as a working pair. A load of 5 N, 9 N, and 13 N and a 5 mm stroke were taken for a test duration of 10 min at a frequency of 3 Hz. The various parameters of the tribological test were obtained by considering ASTM standard G115. The worn surfaces of the monolithic and nanocomposite samples were subsequently analyzed with a 3D profilometer to determine the wear depth, wear breadth, and wear volume of the worn-out samples. For corrosion testing, cylindrical samples (8 mm in diameter and 5 mm long) were put in HBSS for 20 days, and the whole set-up was put in a 37 °C water bath to mimic the temperature of the human body. The solution-to-sample ratio was kept constant at 20 ml:1 cm^2. Furthermore, to remove the corrosion products, a solution containing 20 g CrO_3 and 1.9 g $AgNO_3$ dissolved in 100 ml of de-ionized water was used, which was then observed under FESEM to gain insights into the corrosion mechanisms.

In order to investigate the morphological characteristics of the grains, reinforcement distribution, and interfacial integrity between the matrix and reinforcement, microstructural characterization studies were carried out on metallographically polished extruded samples. Microstructural characterization was performed using high-resolution transmission electron microscopy (HRTEM, Talos F200X G2, Thermo Scientific, USA), field emission scanning electron microscopy (FESEM, Supra 55, Zeiss, Germany) with energy dispersive spectroscopy (EDS) and optical microscopy (OM, Model: DMI Optima, Dewinter Optical Inc, India). The HRTEM samples were prepared by mechanically grinding, punching to a disk 30 μm thick and 3 mm in diameter, and then thinning it with an ion beam. To prepare the samples for OM, a swabbing technique was used to apply an etching solution (5 ml acetic acid, 6 g picric acid, 10 ml water, and 100 ml ethanol) to the samples for approximately 20 s before washing them under running water to reveal the grain boundaries. Before applying the acetic-picral solution, the samples were polished with 500, 1000, 1500, 2000, and 2500 grade sic papers in succession, then mirror polished using diamond paste (1 μm) and alumina (0.5 μm) on a velvet cloth.

3. Results and discussion

3.1. Experimental results

3.1.1. Morphological investigations & structural evolution

To check the quality, shape, and size of the as-received matrix and reinforcing powders, FESEM micrographs have been analyzed as shown in Fig. 3. Fig. 3 shows that the as-received Mg particles possess an irregular morphology, whereas most CNPs are spherical, and some are elongated in nature; these particles are agglomerated. To embed the CNPs uniformly in the Mg matrix and refine the microstructure of the powder samples, 5 h of ball milling were performed. The ball milling time was adopted from the work of Sahed [34], wherein he asserted that a milling time of 5 h was enough to produce an ultra-fine microstructure in the Mg samples. Fig. 4 depicts the morphology of pure Mg and Mg/CeO_2 nanocomposite powders post 5 hr ball milling. From Fig. 4, one can see that the incorporation of CNPs into Mg matrix powders substantially altered the size and morphology of the nanocomposite powders. The average particle sizes of pure Mg, Mg/0.5CeO_2, Mg/1.0CeO_2 and Mg/1.5CeO_2 nanocomposite powders after ball milling were measured to be 255.2, 150.2, 70.7 and 55.4 μm, respectively. Therefore, adding 1.5 vol.% of CNPs resulted in a 78.29% reduction in particle size. The EDX elemental analysis of ball-milled Mg/1.5CeO_2 nanocomposite powder is shown in Fig. 4(f). The peaks corresponding to Mg, Ce, C, and O were observed in Fig. 4(f), validating the distribution of CNPs in Mg particles. Please note that the presence of C in the EDS spectra is primarily attributed to the carbon tape used in the experiment.

Fig. 5 shows the optical micrographs of the extruded unreinforced Mg and Mg/CeO_2 nanocomposites. It should be pointed out that the addition of CNPs in the Mg/1.5CeO_2 nanocomposite substantially decreased the grain size of monolithic Mg. This can be explained by several strengthening factors, including the Orowan strengthening mechanism caused by the restriction of dislocation movement by the reinforcement, the thermal and elastic moduli mismatch between the matrix and reinforcement, which increases dislocation density and thus strength, strong bonding between the reinforcement and the matrix, and adequate load transfer between the matrix and reinforcement.

Fig. 6 shows the results of high-resolution transmission electron microscopy (HRTEM) of Mg/1.0CeO_2 nanocomposites in conjunction with the selected area diffraction (SAD) pattern and energy dispersive X-ray (EDX) mapping. A uniform distribution of CNPs in the Mg matrix can be observed in Fig. 6(a). The creation of moiré fringe patterns due to superimposing one crystal over another can be seen in Fig. 6(b), revealing a discrepancy in the lattice spacing of the crystals. An Mg reflection of $(10\bar{1}1)$ (d spacing = 0.243 nm), a MgO reflection of $(10\bar{1}0)$ (d spacing = 0.277 nm), and a Moiré fringe periodic spacing of 0.93 nm can be seen in Fig. 6(b). The continuous rings, as depicted in Fig. 6(c), demonstrate that high-angle boundaries separated the individual grains and that their alignment is random. In addition, the ring patterns suggest that the size of the grains is in the nanocrystalline range.

3.1.2. Microhardness measurement

Fig. 7 displays the results of the microhardness measurements of pure Mg and Mg/CeO_2 nanocomposites at eight locations along the extruded direction. The locations of hardness testing are depicted in the schematic of Fig. 7. The average Vickers hardness of the pure Mg, Mg/0.5CeO_2, Mg/1.0CeO_2 and Mg/1.5CeO_2 nanocomposites were measured to be 58.6, 68.9, 76.4 and 98.5 kg/mm^2, respectively. It is apparent from Fig. 7 that the addition of CNPs to Mg has improved the

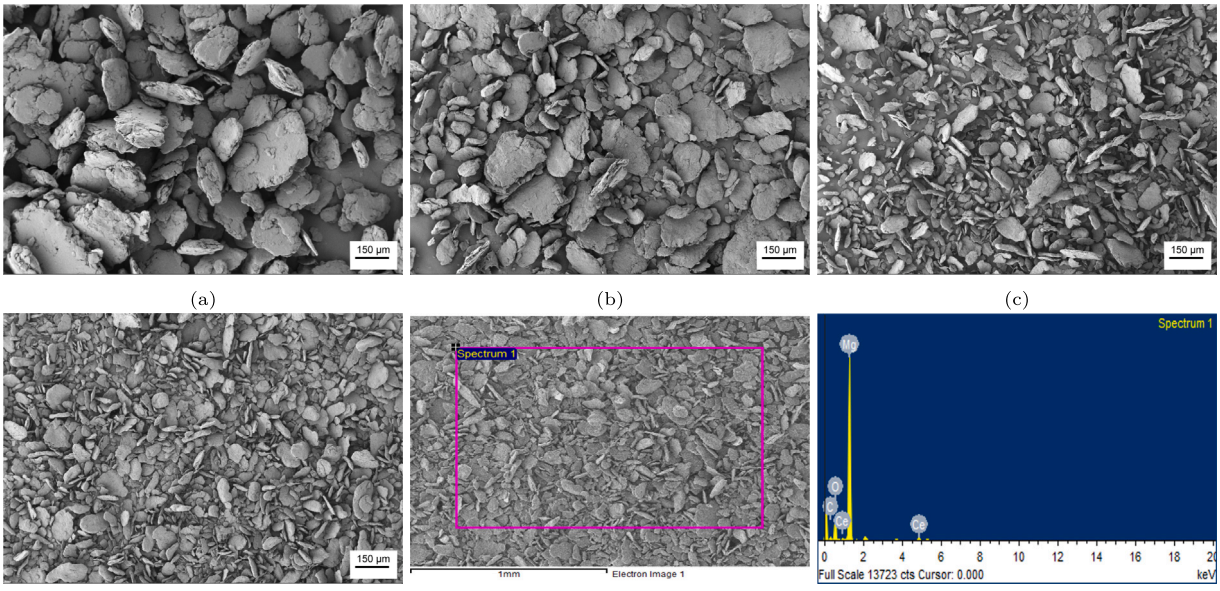

Fig. 4. FESEM micrographs of 5-hour milled powder mixtures of (a) pure Mg, (b) Mg/0.5CeO_2, (c) Mg/1.0CeO_2 and (d) Mg/1.5CeO_2. EDX area analysis of the region shown by the violet box in the FESEM image of Mg/1.5CeO_2 nanocomposite: (e) original picture, (f) the EDS results of color region.

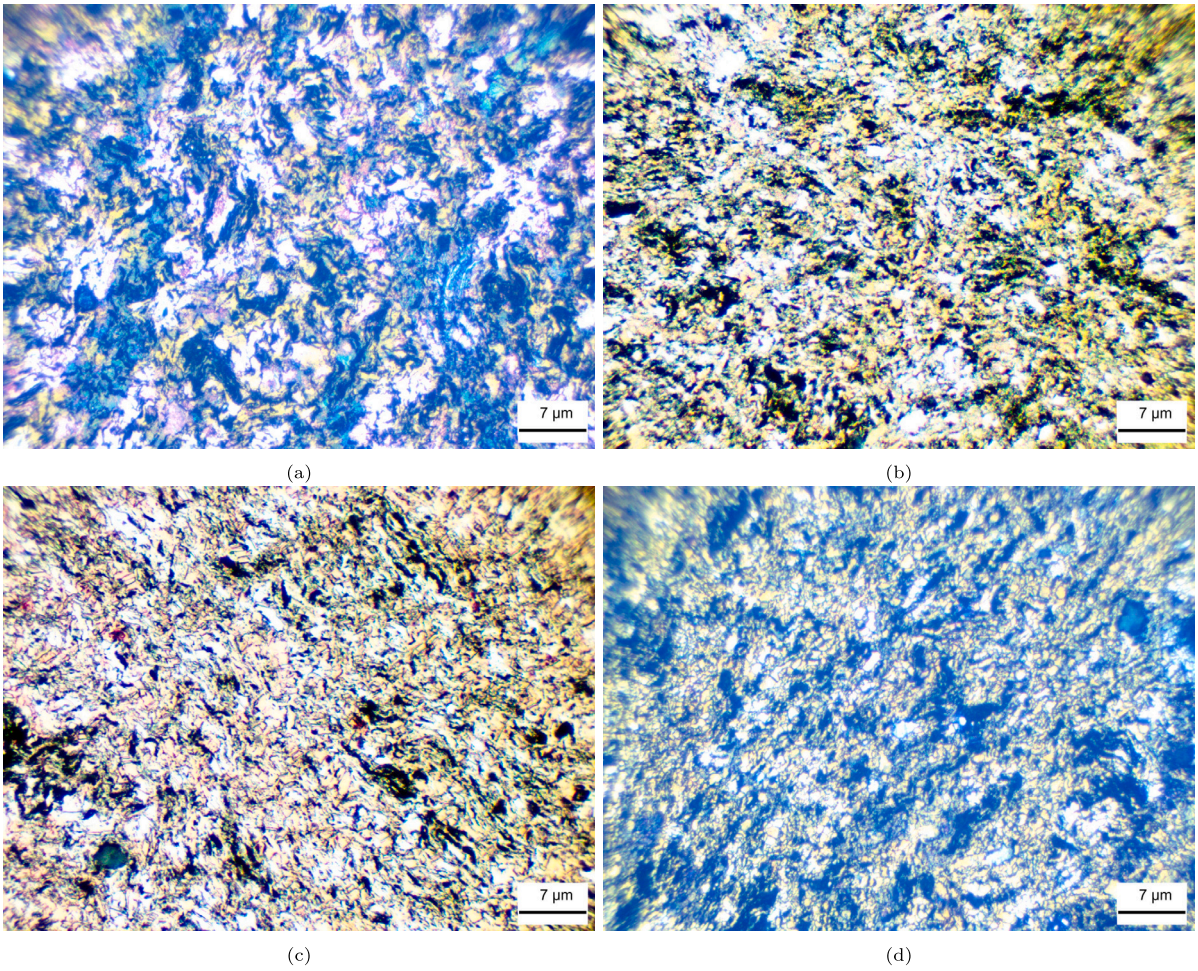

Fig. 5. Optical micrographs showing the microstructure of (a) Pure Mg, (b) Mg/0.5CeO_2, (c) Mg/1.0CeO_2, and (d) Mg/1.5CeO_2 nanocomposites.

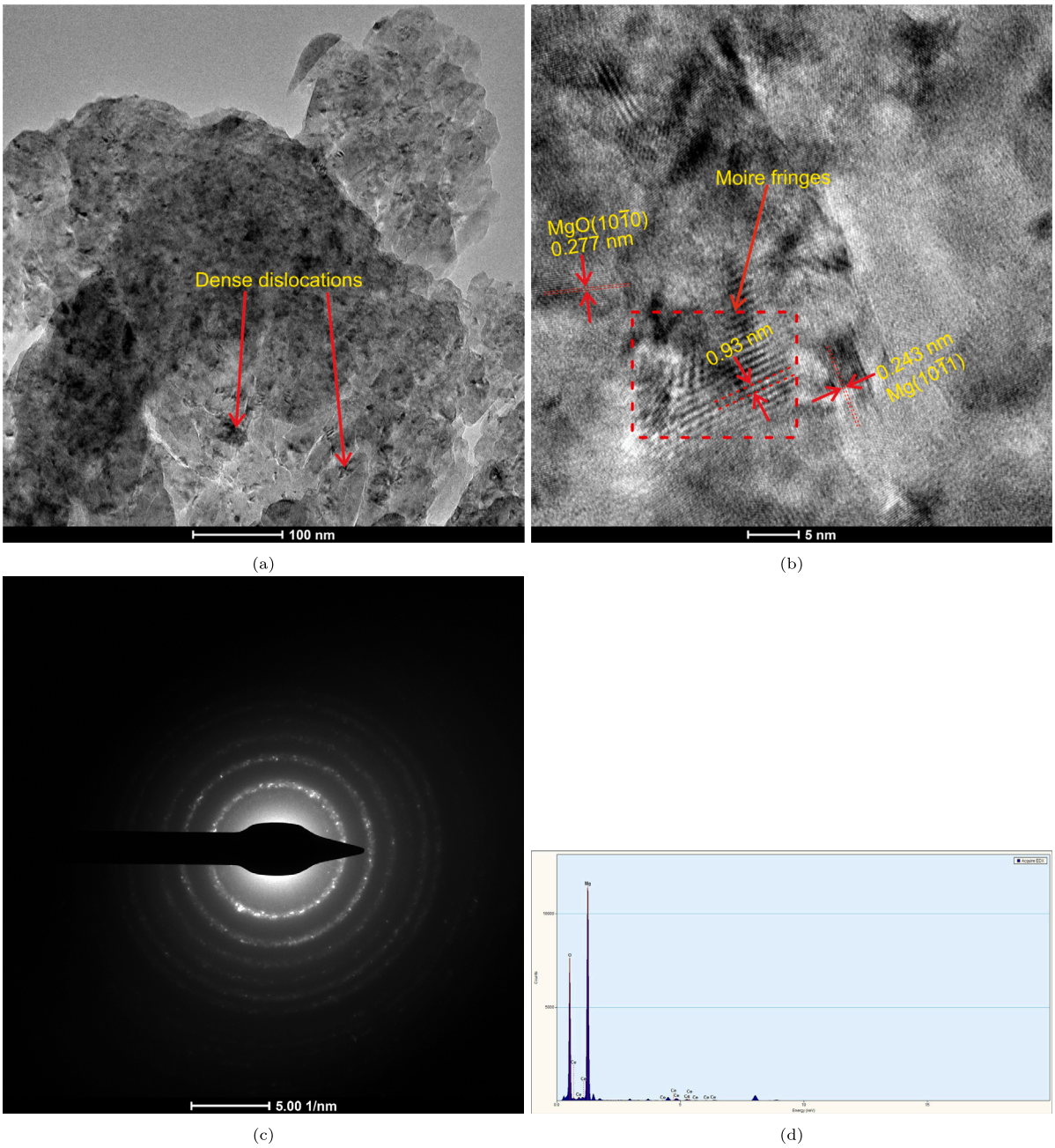

Fig. 6. HRTEM image of the Mg/1.0CeO_2 nanocomposites showing (a) CNP distribution in the Mg matrix, (b) high-resolution image showing Moire fringes, Mg(10$\bar{1}$1) and MgO(10$\bar{1}$0) phase, (c) associated SADP pattern of Fig. 6(b), and (d) EDX area mapping of Fig. 6(b).

hardness of the nanocomposites. Mg/1.5CeO_2 nanocomposite exhibited a significant increase in the hardness value from 58.6 to 98.5 kg/mm^2 (an increase of about 68.1%). Moreover, hardness measured at different positions along the extrusion direction for monolithic Mg, Mg/0.5CeO_2, and Mg/1.0CeO_2 nanocomposites revealed no significant differences, indicating two phenomena: (a) a uniform dispersion of the CNPs in the Mg matrix and (b) uniform strain distribution during hot extrusion. However, at a higher volume percent of CNPs (1.5 vol.%), a slight variation in the hardness values across locations can be seen, which could be due to the agglomeration of particles at higher volume fractions. A similar observation regarding the hardness behavior of the Mg-based nanocomposites was reported by Akbaripanah et al. [35].

Several mechanisms have been proposed to explain the improvement in the hardness of the nanocomposites [1,3,15,26]. Grain refining and the presence of CNPs are likely the main mechanisms functioning here [6]. Also, the Orowan strengthening mechanism may increase hardness due to the uniform dispersion of NPs in the matrix [26]. Additionally, certain additional mechanisms involving the mismatch of the thermal expansion coefficient between the matrix and the reinforcements and the load transfer strengthening mechanism may be considered the other contributors to the increased microhardness [23].

3.1.3. Tribomechanical properties

A reciprocating wear test was employed to assess the tribological characteristics of Mg/CeO_2 nanocomposites containing varying concentrations of CNPs. Normal loads of 5 N, 9 N, and 13 N were employed to evaluate the friction and wear characteristics of the developed composites.

Fig. 8 shows the friction coefficient (COF) for the monolithic Mg and Mg/CeO_2 nanocomposite samples under the applied loads of 5, 9,

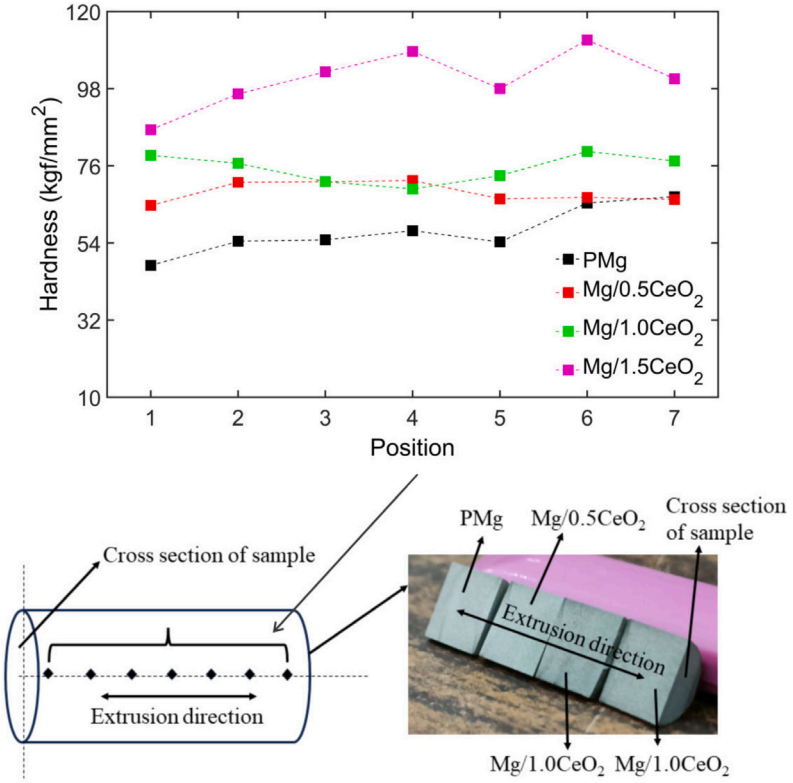

Fig. 7. Vickers microhardness measured along the extrusion direction as shown in the schematic diagram. The distance between the points was taken as 0.5 mm.

and 13 N. The fluctuations in Fig. 8 could be due to the effects of severe adhesive wear mechanisms. It could also be caused by the accumulation and removal of wear debris on the surface's worn tracks [36], local adhesion and detachment [37], and generation of frictional heat [38]. It is important to note that COF values reported in Fig. 8(e) were calculated by averaging the experimental data corresponding to the data presented in Fig. 8. In Fig. 8(e), a distinct drop in the COF values can be seen with the increase in the applied load. This could be attributed to higher local frictional heat due to increased applied load, which promoted the oxidative wear mechanism. Therefore, a rise in oxidation was likely the second factor that lessened the significance of adhesion and, as a result, lowered the COF value [38]. Moreover, it can be seen that Mg/CeO_2 nanocomposites exhibited significantly better frictional properties than pure Mg, and the COF value of nanocomposites increased proportionally with reinforcement addition. The difference between the COF values for pure Mg and Mg/CeO_2 nanocomposites was more pronounced at the load of 13 N. At the applied load of 13 N, the COF was 0.207 for Mg/1.5CeO_2, 0.209 for Mg/1.0CeO_2, 0.229 for Mg/0.5CeO_2, and 0.234 for pure Mg. Thus, the COF of Mg/1.5CeO_2 was enhanced by 11.5% compared to pure Mg. This was due to hard, tough, wear-resistant CNPs and the strong bonding between the reinforcement and the matrix [15]. Hence it can be concluded that the addition of CNPs significantly improved the wear resistance of the nanocomposites.

Figs. 9a–d shows the 3D wear track morphology of the pure Mg and Mg/CeO_2 nanocomposites at loads of 5, 9, and 13 N, respectively. The figures show that the 3D profile of the wear track of the pure Mg at all three loads showed a uniform wear track (Fig. 9(a)). A similar near-uniform nature can be seen for the Mg/CeO_2 nanocomposites at low applied loads. However, it exhibited a non-uniform wear track at higher loads and higher volume percent of ceria nanoparticles (Fig. 9(d)). The wear rate results of the pure Mg and Mg/CeO_2 nanocomposites at different loads are shown in Fig. 10. Fig. 10 showed that increasing the CNP content in the nanocomposites resulted in a lower wear rate in the samples. This phenomenon occurs due to the presence of reinforcing particles within the Mg matrix and their correct bonding and distribution throughout the matrix. These elements support the bulk of the stress placed on the sample, which increases wear resistance. The monolithic Mg sample at a 13 N load showed the maximum wear rate, which was 37.73, 22.28, and 10.68% greater than the Mg/1.5CeO_2, Mg/1.0CeO_2 and Mg/0.5CeO_2 nanocomposite, respectively. Furthermore, it is evident from Fig. 10 that the wear rate of the pure Mg and nanocomposite samples increases with an increase in the applied load. The wear rate value of pure Mg, Mg/0.5CeO_2, Mg/1.0CeO_2 and Mg/1.5CeO_2 increased by 76.50, 77.38, 61.99 and 59.01%, respectively, from 5 to 13 N. This can be attributed to the samples' subsurface deformation, crack nucleation, and crack propagation as a result of the increased load, which causes higher wear [39]. This may also be due to the minimal occurrence of nanoparticle agglomeration. The uniform dispersion of these nanoparticles efficiently distributes the applied load and mitigates surface contact stresses, consequently improving the wear resistance of the nanocomposites. Agglomeration represents a pivotal concern in magnesium nanocomposites. Agglomeration of the nanoparticles within the magnesium matrix can lead to localized areas of weakness. These agglomerated regions become more susceptible to wear, as they give rise to stress concentrations and foster the formation of microstructural flaws, such as voids or cracks, which, in turn, serve as initiation sites for wear-related processes [40,41].

In accordance with the 3D surface morphologies, the 2D cross-sectional profile of the wear track was acquired at five distinct locations, as shown in Figs. 11–14. Figs. 11–14 also depicts the width and depth of the wear track corresponding to the five locations in the 2D wear track diagram. The results show that the wear width and depth were lower for the Mg/CeO_2 nanocomposites compared to monolithic Mg. The average wear depth of pure Mg at the applied loads of 5, 9, and 13 N was reported to be 42.1, 62.8, and 62.9 μm, respectively. Hence, in comparison with pure Mg, one could notice a significant decrease in the average wear depth, i.e., of 23.04, 19.58, and 14.78%, for Mg/1.5CeO_2 at the respective loads. Furthermore, when compared

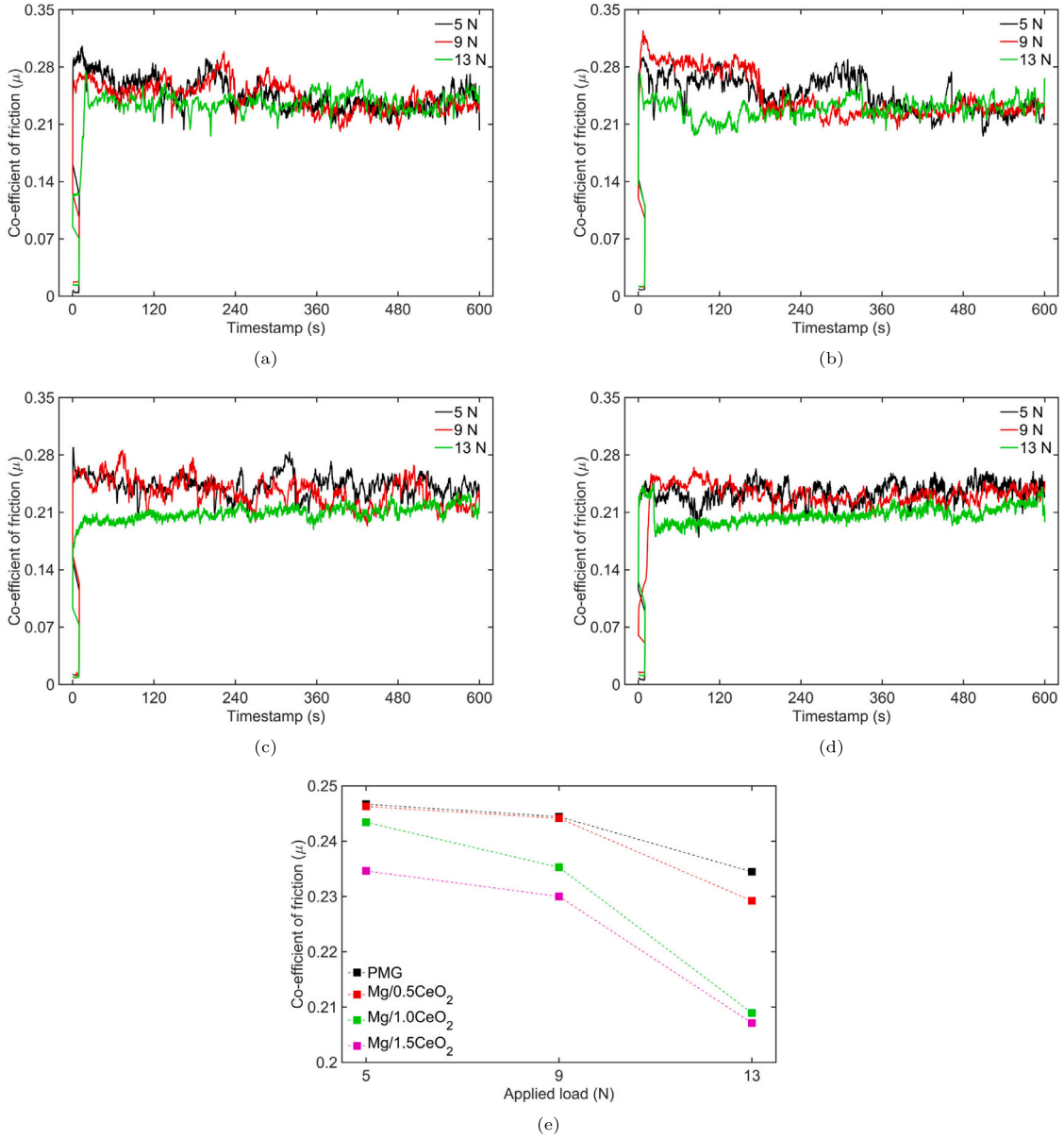

Fig. 8. The variation of the COF with the sliding wear time for (a) pure Mg, (b) Mg/0.5CeO_2, (c) Mg/1.0CeO_2, (d) Mg/1.5CeO_2 nanocomposites and (e) COF values of the samples.

to pure Mg, the width of the wear track of Mg/1.5CeO_2 nanocomposite was reduced by 8.06, 12.50, and 20.21% at loads of 5, 9, and 13N. A comparison between Fig. 11 and Fig. 14 revealed a noticeable change in the appearance of wear depth profiles. The wear depth plots for the Mg/1.5CeO_2 nanocomposite exhibited varied wear depth profiles at different cross-sections; however, the variation for the monolithic Mg was minimal. This could be due to the formation of uneven valleys due to the rubbing action of the steel ball with the matrix and reinforcement nanoparticles for the nanocomposites. The summary of the tribological characteristics in terms of the wear width and depth has been presented in Table 2.

In order to examine the effect of the addition of rare-earth reinforcement on the wear characteristics of Mg/CeO_2 MMNCs, worn-out surfaces of pure Mg and Mg/CeO_2 nanocomposites were analyzed under room temperature conditions using FESEM, as shown in Fig. 16. Fig. 16 demonstrate evidence of abrasion, delamination, ploughing, microcracks, and oxide wear mechanisms in the composite. The abrasive wear is associated with the formation of grooves parallel to the sliding direction under load. At low loads, abrasive wear was characterized by shallow scratches and numerous grooves that ran parallel to the sliding direction, as illustrated in Fig. 16(a), Fig. 16(d) and Fig. 16(g). In addition to abrasion, the presence of the delamination wear mechanism can also be observed at low loads. However, its presence became more pronounced at higher loads. The delamination wear mechanism can be explained by the following: as sliding contact time and load increase, wear stresses due to siding increase, causing the contact surface to deform into a thin layer with increased strains and temperatures; further sliding causes strains to develop at these thin layers, which results in their separation, i.e., the wear delamination mechanism. It is also important to note that the oxidation wear mechanism becomes more apparent at higher loads. This can be attributed to the frictional heating of surfaces during the repeated sliding of the balls over the sample surface. The formation of an oxide layer was observed by energy dispersive spectroscopy (EDS) and is shown in Fig. 15(b). The formation of oxide layers on the surface of the samples protects them from wear and lowers the wear rate. Another important mechanism observed at higher loads is the ploughing of the surfaces. This is primarily due to the formation of wear debris during the final stage of the delamination

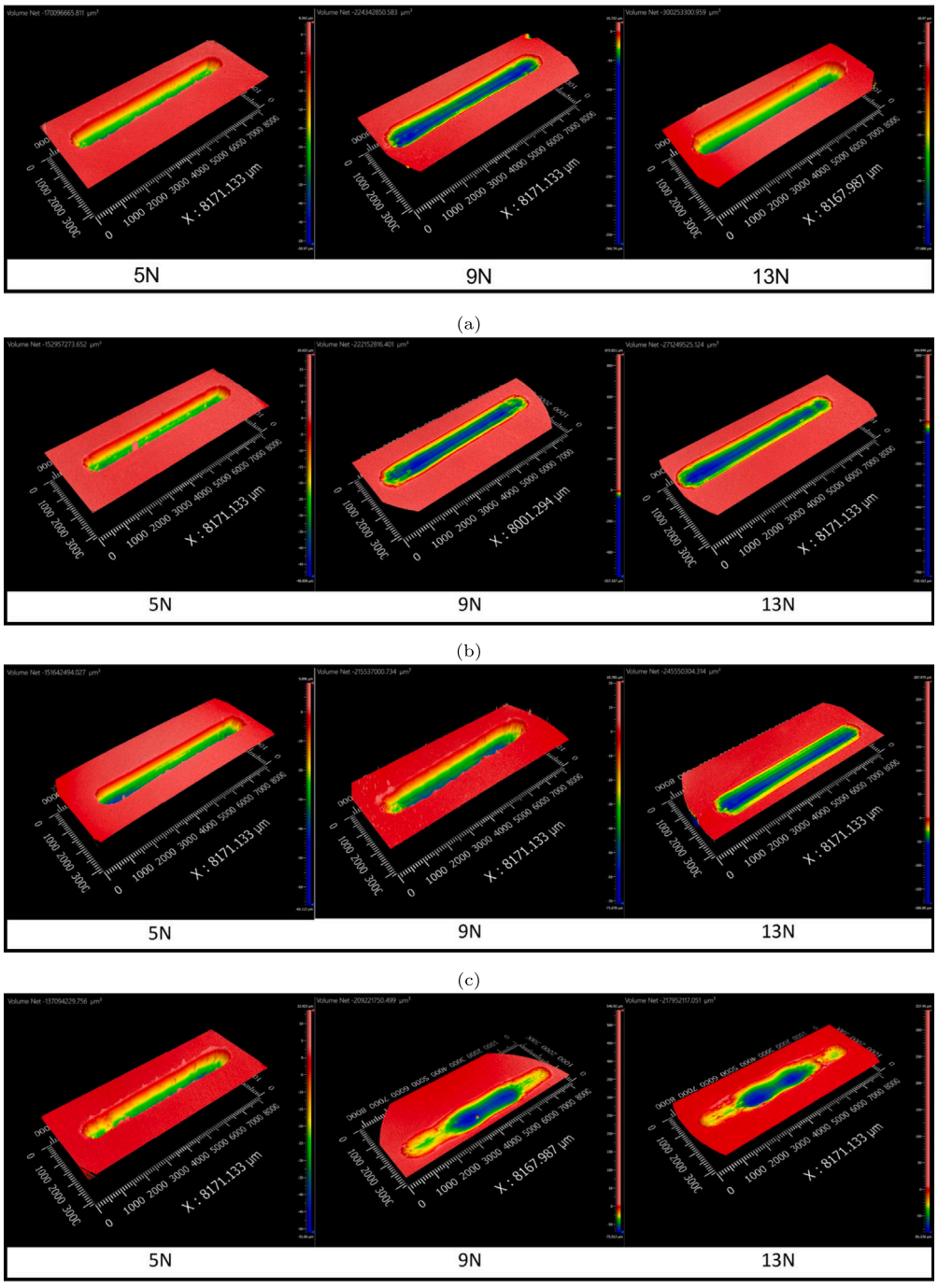

Fig. 9. The 3D worn-out wear track of the (a) base Mg, (b) Mg/0.5CeO_2, (c) Mg/1.0CeO_2, (d) Mg/1.5CeO_2 nanocomposite at 5, 9, and 13 N load.

theory [42]. The size of the debris particles increases with increasing load, and this causes the formation of plough with large groove width. As can be observed from Fig. 16, the wear surface morphology of the Mg/CeO_2 nanocomposites is different from that of the monolithic Mg. When the reinforcement content varied from 0.5 vol.% to 1.5 vol.%, the worn-out surfaces of the nanocomposites revealed narrower grooves and nearly flat surfaces. This is particularly evident in Fig. 16(h) and Fig. 16(k). These findings confirm the nanocomposites' decreased wear volume loss and suggest the characteristics of a mild wear process. Another notable feature that can be observed in all the samples is the enlargement of the grooves of the worn surfaces as the applied load increased from 5 to 13 N. This is also accompanied by the breakdown of the agglomerated wear debris on the worn surface and the increased localized plastic deformation due to the increased load. A uniform distribution of the fine debris particles resulting from the breakdown of agglomerated wear debris is shown in Fig. 16(i).

3.1.4. Corrosion measurement

Mg-based materials must have good corrosion resistance to maintain mechanical integrity during the healing period with minimal inflammatory reaction to be effectively targeted as a biodegradable implant. Mg is a very active element in the periodic table. Mg-based materials are susceptible to corrosion in the HBSS solution at pH 7.4. Mg-based materials degrade electrochemically in an aqueous environment, producing

Table 2
Summary of the wear characteristics of monolithic Mg and Mg/xCeO_2(x = 0.5, 1, and 1.5) nanocomposites at applied loads of 5, 9, and 13 N.

Materials	Applied load					
	5 N		9 N		13 N	
	Wear width (μm)	Wear depth (μm)	Wear width (μm)	Wear depth (μm)	Wear width (μm)	Wear depth (μm)
Pure Mg	916.4	42.1	1136.2	62.8	1183.4	62.9
Mg/0.5CeO_2	857.3	41.3	1077.1	53.2	1054.6	56.5
Mg/1.0CeO_2	849.4	40.3	1031.1	51.9	1003.3	55.5
Mg/1.5CeO_2	842.5	32.4	994.1	50.5	944.2	53.6

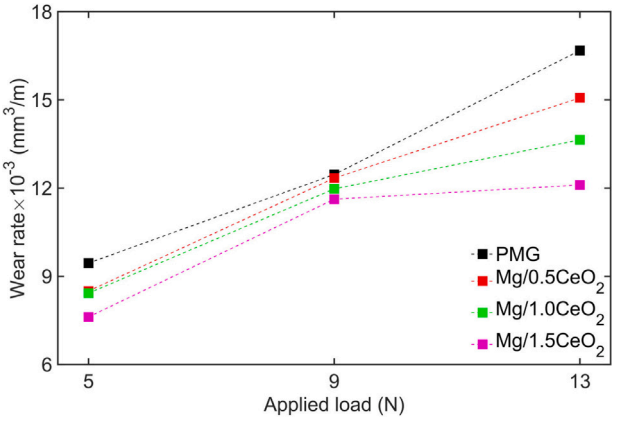

Fig. 10. Wear rate of the pure Mg and nanocomposite samples under varying load.

magnesium hydroxide and hydrogen gas. The release of hydrogen gas, which can lead to the formation of gas pockets, can hinder the healing process and could be prevented by regulating the corrosion rate.

One of the most popular methods for analyzing the corrosion behavior of implants is immersion testing. In the current investigation, four samples from all combinations (Pure Mg, Mg/0.5CeO_2, Mg/1.0CeO_2, Mg/1.5CeO_2) were ground and assessed prior to immersion to guarantee consistent surface condition. To simulate the body's environment, the samples were immersed in HBSS at 37 °C by using a water bath. The samples were immersed in HBSS for 20 days. The pH value of the simulated fluid and loss of weight of the samples were recorded after 1, 4, 6, 7, 13, 16, and 20 days. The corrosion rate was computed using the following relationship:

$$\text{Corrosion Rate (mm/year)} = \frac{K \times (W_B - W_A)}{\rho A T} \quad (1)$$

where K, W_B, W_A, ρ, A, and T represent the time conversion coefficient (8.76×10^4), pre-immersion sample weight (g), post-immersion sample weight (g), the density of the sample (g/cc), the immersed surface area of the sample (cm^2) and sample immersion time (hr), respectively.

Fig. 17 illustrates corrosion rate and pH measurement of immersed unreinforced Mg and Mg/CeO_2 nanocomposites as a function of immersion time. Fig. 17(a) shows a drastic increase in pH value at the start of the corrosion cycle (day 1). The high value of the initial pH can be due to Mg and Mg-based materials interacting with their physiological surroundings, with high interactions reported during the first 12–24 h [43]. However, the pH measurements for all the samples reached dynamic stabilization post-completion of the initial corrosion cycle until the end of the cycle at 20 days. The absolute pH values of the Mg/CeO_2 nanocomposites were lower than those of pure Mg, as shown in Fig. 17a. This implies that the uniform presence of the CNPs resulted in improved dynamic passivation of the composite samples, thereby keeping pH changes under control. Similarly, the corrosion rate of all the samples was high towards the end of day 1, with slight variations around the end of day 7. However, a nearly uniform or decreasing trend could be observed until the end of the 20-day cycle. As shown in Fig. 17b, the corrosion rate for pure Mg at the end of day 20 was about 2.75 mm/y. The high value of the corrosion rate of Mg agrees with the FESEM micrographs depicting the formation of noticeable big pits and cracks on the surface, as can be seen in Fig. 18. However, the corrosion rate of the nanocomposites was lower than that of unreinforced Mg, with Mg/1.0CeO_2 nanocomposite displaying the lowest value at 1.72 mm/y (37.46% lower than pure Mg). This enhancement in corrosion resistance can be attributed to the incorporation of REO NPs into the Mg matrix and their uniform dispersion, effectively mitigating the formation of NP agglomerates. The phenomenon of agglomeration represents a critical concern in the domain of Mg nanocomposites, demanding diligent consideration and preventative measures. The agglomeration of NPs has been shown to promote uneven pitting and faster corrosion within metal matrices, consequently diminishing the overall corrosion resistance of materials [2]. This study further emphasizes the adverse effects of NP agglomeration on material strength properties, thereby exacerbating the corrosion characteristics. In addition, the research conducted by Sahoo [44] has provided evidence that nanoparticle (NP) agglomeration opens up cathodic sites, thereby amplifying the galvanic effect, and resulting in an escalation of corrosion rates.

The difference in corrosion behavior between monolithic Mg and Mg/CeO_2 nanocomposites can be explained by the chemical reactions between the Mg^{2+}, OH^-, and Cl^- that exist in the HBSS, as described in Eqs. (2)–(6), which control the corrosion process of the samples.

$$Mg + 2H_2O \rightarrow Mg(OH)_2 + H_2 \quad (2)$$

$$Mg \rightarrow Mg^{2+} + 2e^- \quad \text{Anodic reaction} \quad (3)$$

$$2H_2O + 2e^- \rightarrow 2OH^- + H_2 \quad \text{Cathodic reaction} \quad (4)$$

$$Mg^{2+} + 2OH^- \rightarrow Mg(OH)_2 \quad \text{Chloride attack} \quad (5)$$

$$Mg(OH)_2 + Cl^- \rightarrow MgCl_2 + 2OH^- \quad \text{Chloride attack} \quad (6)$$

$$10Ca^{2+} + 8OH^- + 6HPO_4^{2-} \rightarrow Ca_{10}(PO_4)_6 + 6H_2O \quad \text{Apatite biomineralization} \quad (7)$$

$$10Ca^{2+} + 2OH^- + 6HPO_4^{2-} \rightarrow Ca_{10}(PO_4)_6 \quad (8)$$

$$3Ca^{2+} + 2OH^- + 2PO_4^{3-} \rightarrow (Ca)_3(PO_4)_2 \quad (9)$$

The anodic breakdown of Mg into Mg^{2+} results in a higher corrosion rate and high pH values at the initial corrosion cycle (day 1). This dissolution at the anode translates into the creation of hydrogen gas pockets on the surface of samples [9]. Furthermore, the ionic interaction between Mg^{2+} and OH^- results in the formation of a protective porous $Mg(OH)_2$ layer. The formation of the honeycomb $Mg(OH)_2$ film is shown in the inset figure of the Mg/1.0CeO_2 nanocomposite at the end of the 6th day (Fig. 18). This development of the $Mg(OH)_2$ layer could assist in stabilizing the corrosion rate and pH values of the produced nanocomposites, as seen in Fig. 17(a) and Fig. 17(b). The XRD analysis, which can be seen in Fig. 19, corroborated the formation of the $Mg(OH)_2$ layer on the surface of the samples. Also, it is commonly

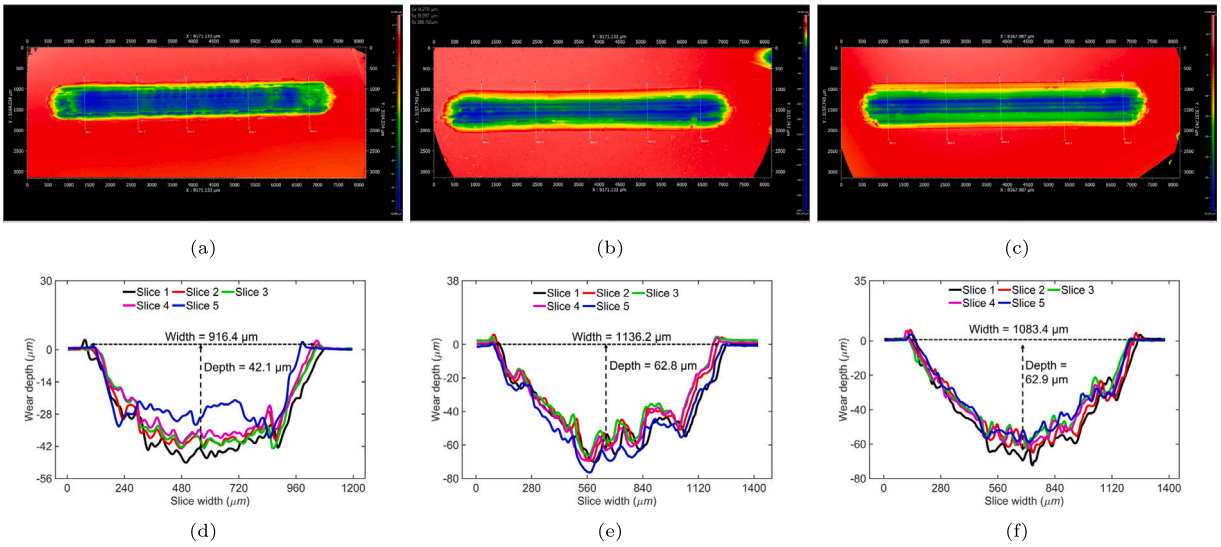

Fig. 11. The 2D cross-sectional wear tracks, width, and depth profiles at five locations of the PMg corresponding to (a,d) 5 N, (b,e) 9 N and (c,f) 13 N.

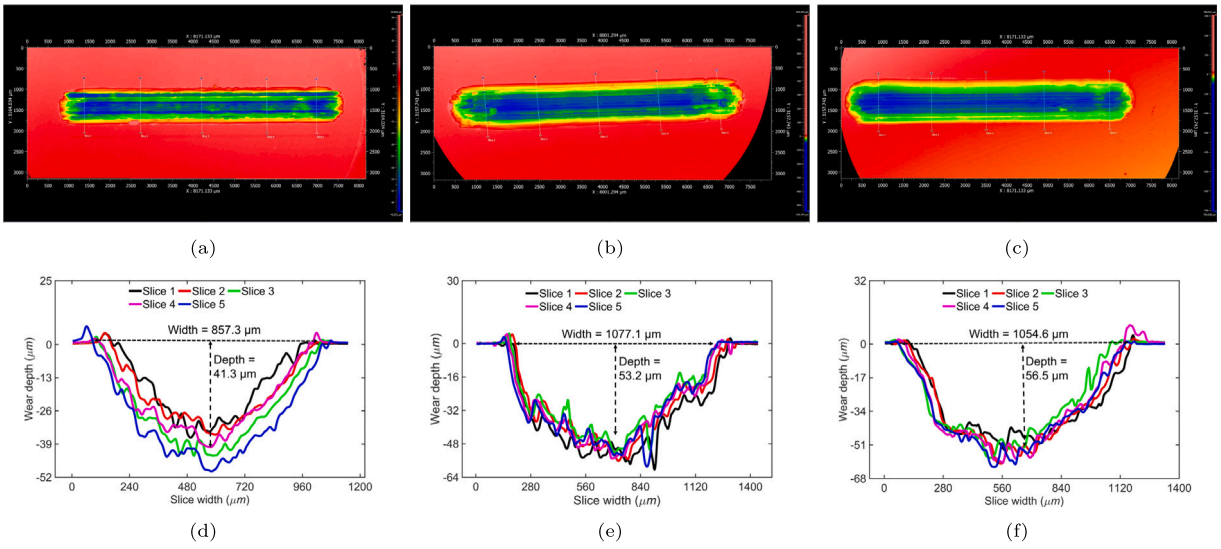

Fig. 12. The 2D cross-sectional wear tracks, width and depth profiles at five locations of the Mg/0.5CeO_2 nanocomposite corresponding to (a,d) 5 N, (b,e) 9 N and (c,f) 13 N.

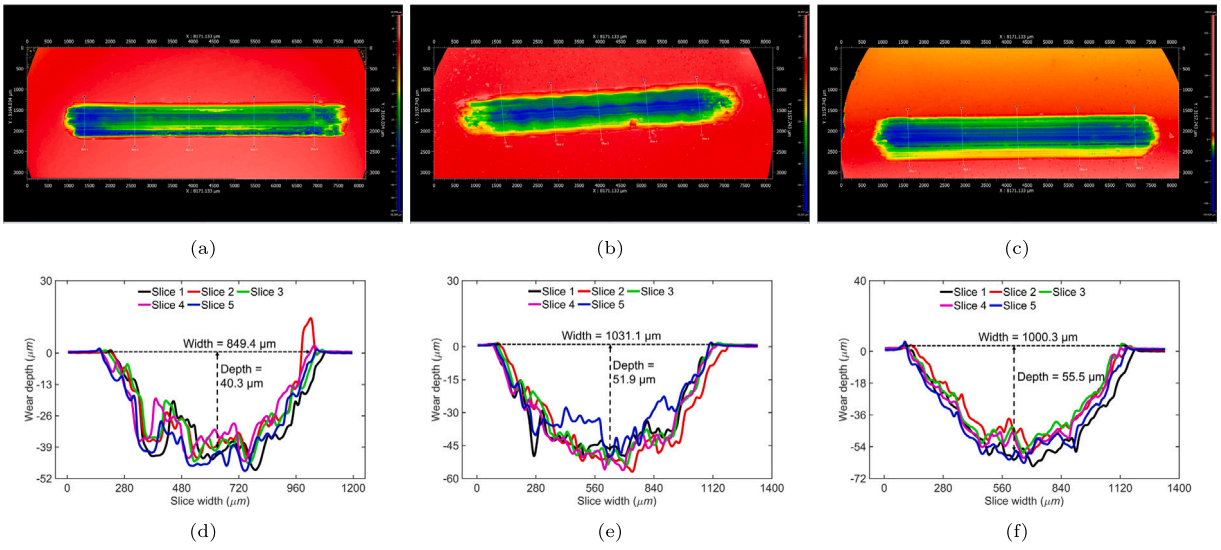

Fig. 13. The 2D cross-sectional wear tracks, width and depth profiles at five locations of the Mg/1.0CeO_2 nanocomposite corresponding to (a,d) 5 N, (b,e) 9 N and (c,f) 13 N.

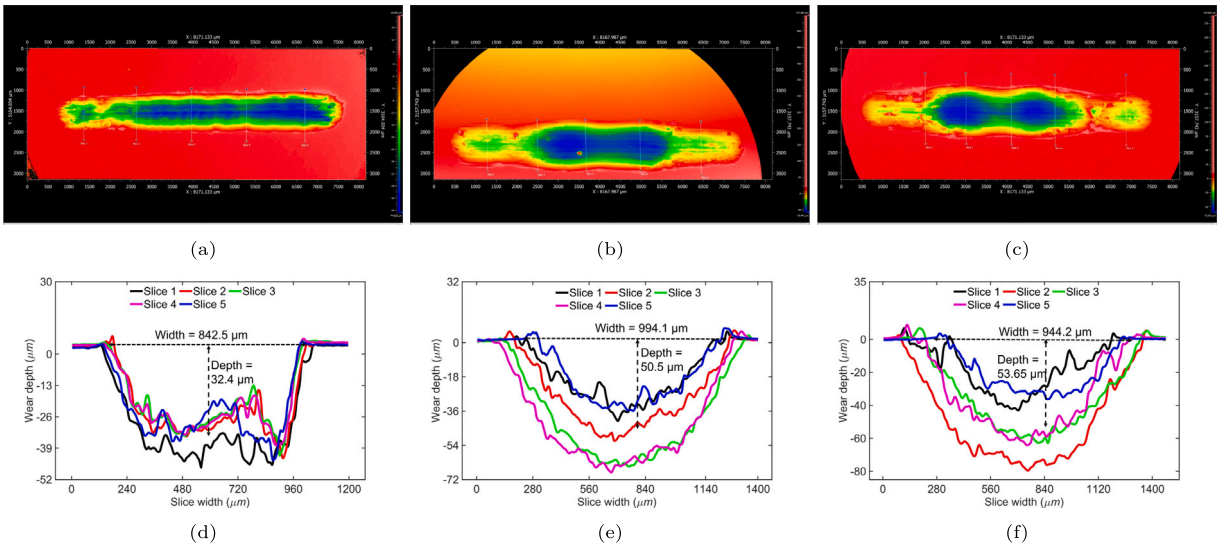

Fig. 14. The 2D cross-sectional wear tracks, width and depth profiles at five locations of the Mg/1.5CeO_2 nanocomposite corresponding to (a,d) 5 N, (b,e) 9 N and (c,f) 13 N.

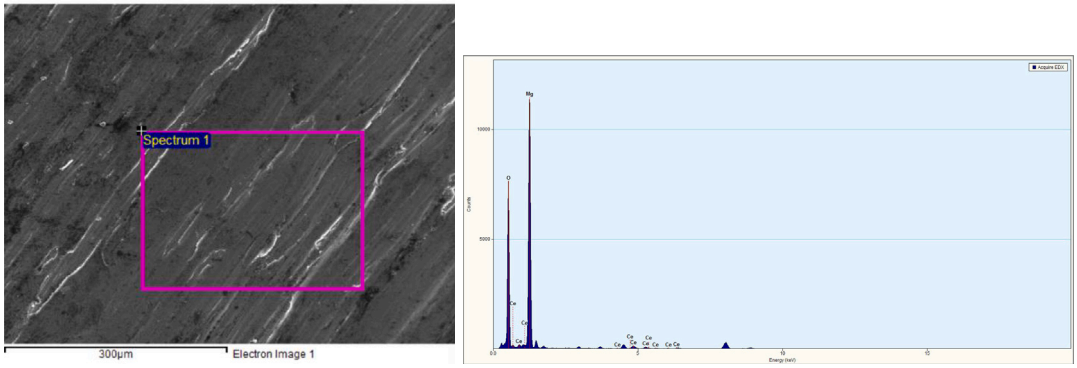

Fig. 15. (a) FESEM wear micrograph of the Mg/1.0CeO_2 nanocomposite at 5 N load and (b) EDS analysis of the selected area.

recognized that Mg has low corrosion resistance in chloride environments, and the presence of Cl^- ions in the HBSS solution accelerates the process of corrosion by producing $MgCl_2$ [9]. This causes a rise in the concentration of OH ions in the solution and the deterioration of the hydroxide layer. In the present work, mechanical attrition and the incorporation of ceria nanoparticles considerably reduced the grain size of pure Mg. As a result of microstructure refinement, there are more grain boundaries with higher energies, which facilitate surface reactivity and accelerate the formation of the protective layer [45]. This reduces the degree of localized corrosion. In addition to microstructure refinement, the reduced porosities reported in the nanocomposite samples may also help mitigate the effect of corrosion [9]. The improvement of corrosion protection is also supported by the absence of secondary phases or impurities in the material that could act as stress concentration sites and cause stress corrosion cracking.

Fig. 18 presents the findings of the FESEM analysis of the corroded surface of the pure Mg and Mg/CeO_2 nanocomposite samples at the end of days 1, 5, and 20 (with corrosion products). From Fig. 18, the formation of white residues on the surface of the samples after 1-day immersion can be seen. A high-resolution FESEM image of the formation of the white residue is encapsulated in the inset figure of pure Mg at the end of the first day. These precipitations appeared to minimize local corrosion attacks and result in more uniform corrosion in Mg/CeO_2 nanocomposites, whereas uncovered regions of the samples demonstrated significant corrosion rates. The formation of cross-linked cracks on all the samples can be seen after six days of immersion due to moisture removal from the corrosion film. Pure Mg samples, in comparison to Mg/CeO_2 nanocomposites, accumulated more cracks on the surface, as shown in Fig. 18 (Day 20).

Fig. 19 displays the XRD patterns of the corroded surfaces of pure Mg and Mg/CeO_2 nanocomposites post 14 days of immersion in HBSS. Results from XRD analysis demonstrated the formation of $Mg(OH)_2$, MgO, and $CaMg(CO_3)_2$ on the surface of the samples. Furthermore, the broadening of the peaks can be seen in Fig. 19, which could be due to amorphous corrosion products' existence. An EDS analysis of the Mg/1.0CeO_2 sample was also conducted to determine the quantitative presence of prominent elements after 20 days of immersion. As shown in Fig. 20, the mapping findings demonstrated the presence of Mg, Ce, O, Cl, Ca, P, and Na. This suggested the formation of the quasi-adherent layer as a result of chloride assault and the formation of the hydroxide layer. Another interesting result from the EDX analysis is the Ca:P ratio, which was identified as 1:1.87. This value is close to the Ca:P ratio required for bone mineralization (1:1.67) [46]. This indicated the promising bioactivity of the nanocomposites. The formation of the spherical calcium phosphate precipitates on the surface of the Mg/1.0CeO_2 nanocomposite is shown in the inset figure of Mg/1.0CeO_2 at the end of the 20th day (Fig. 18). Therefore, it is clear that the effective biomineralization of the nanocomposites is greatly influenced by the synergistic relationship between the presence of CNPs and microstructure refinement [47]. The degree of mineralization improved following the increase in immersion time, and it is anticipated that

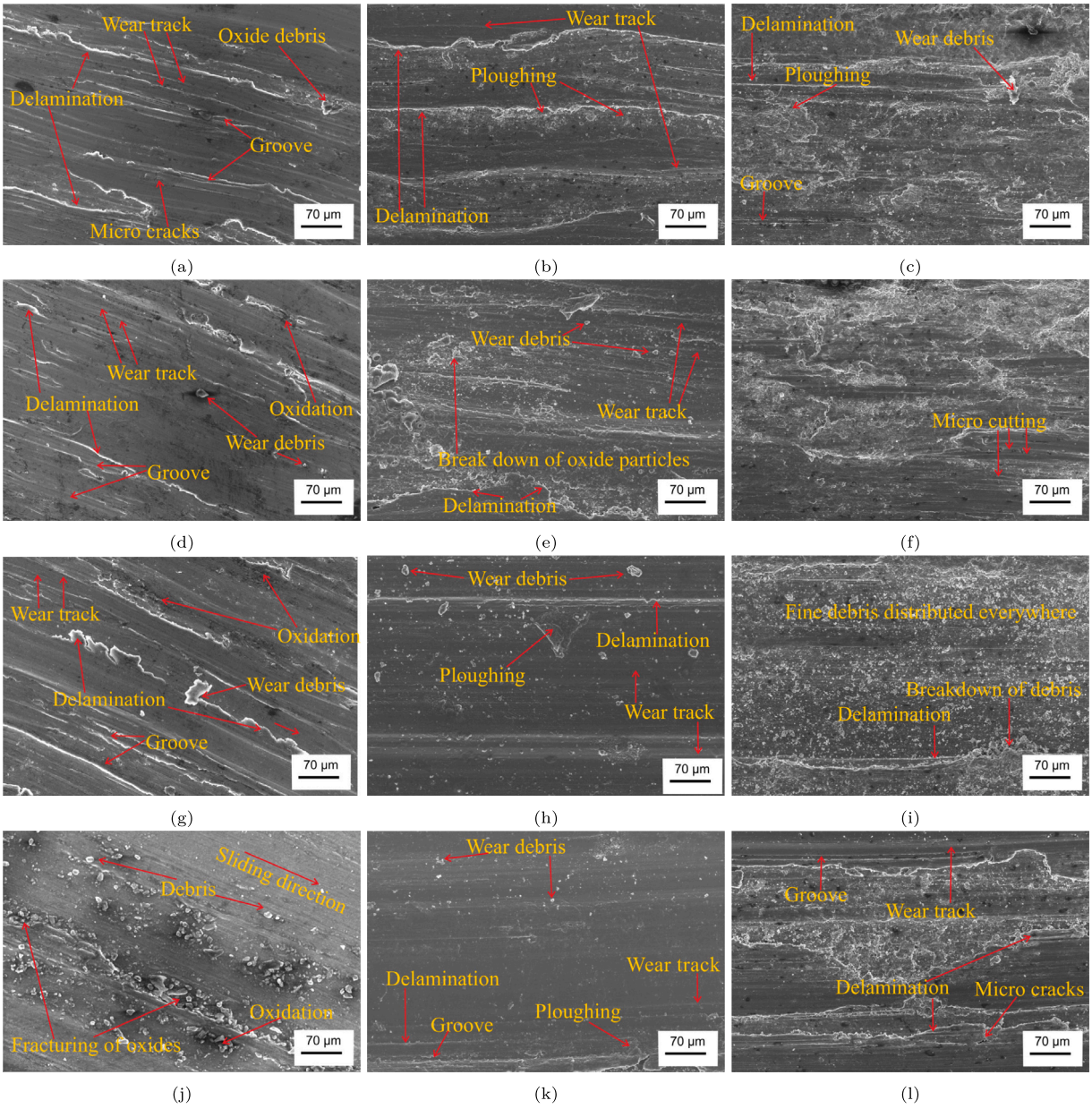

Fig. 16. FESEM of worn surface of (a–c) pure Mg, (d–f) Mg/0.5CeO_2, (g–i) Mg/1.0CeO_2 and (j–l) Mg/1.5CeO_2 at loads of 5, 9, and 13 N, respectively.

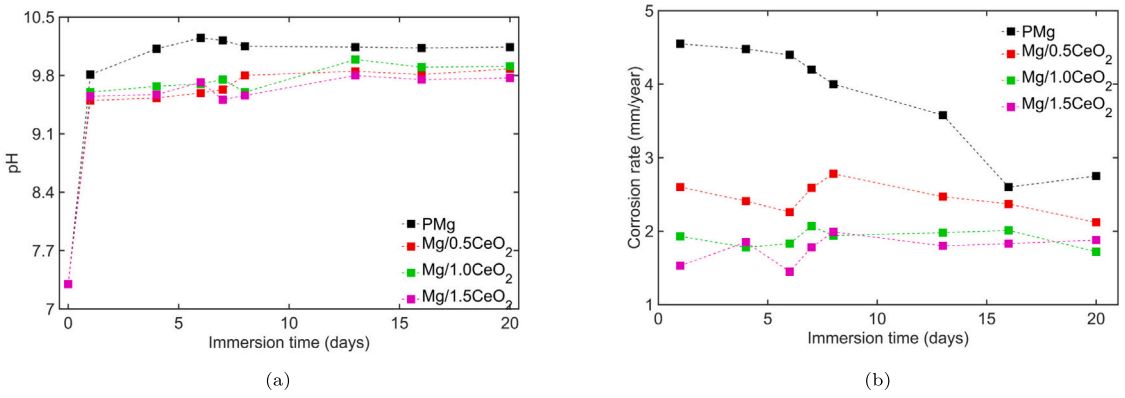

Fig. 17. (a) pH of the immersion testing and (b) corrosion rates of monolithic Mg and Mg/CeO_2 nanocomposite with immersion time.

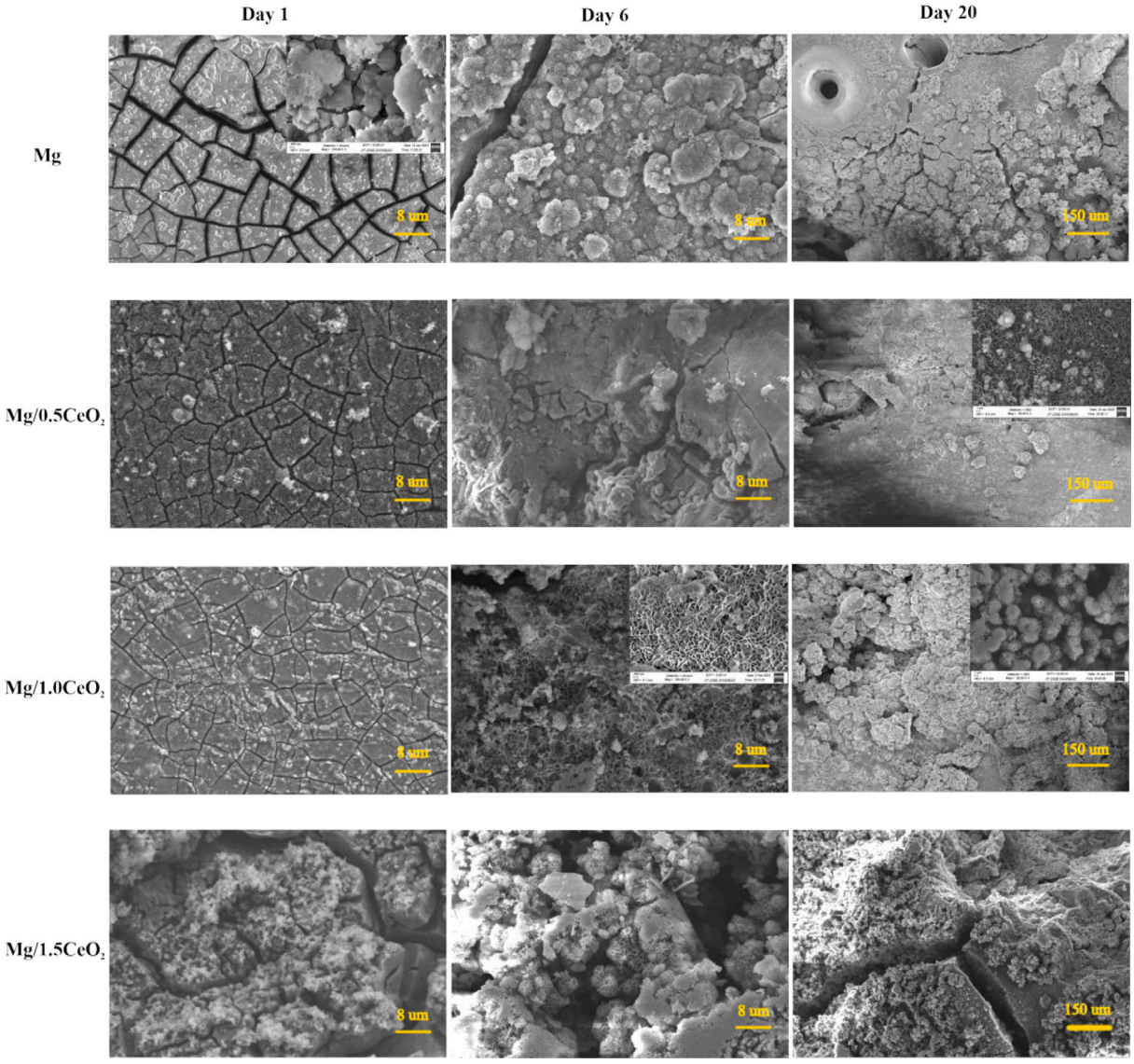

Fig. 18. FESEM analysis of unreinforced Mg and Mg/CeO_2 nanocomposites immersed in HBSS at the end of day 1, 6 and 20.

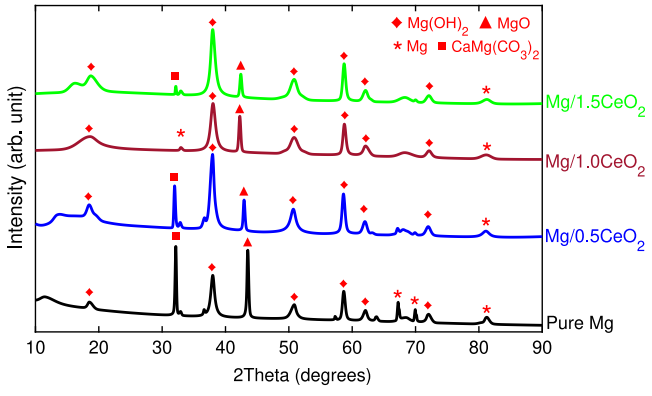

Fig. 19. XRD analysis of the monolithic Mg and Mg/CeO_2 nanocomposites after immersion in HBSS for 14 days.

the implant surface will spontaneously produce healthy bones with live tissue [48].

FESEM analysis of post-corroded pure Mg and Mg/CeO_2 samples, taken on the 20th day after the corrosion products were removed, is depicted in Fig. 21. As illustrated in Figs. 21a–d, it can be seen that the pure Mg and nanocomposites displayed micron-sized pillars surrounded by sizable holes suggesting a great deal of galvanic assault in HBSS. The development of surface cracks is also evident in all of the samples. This could be ascribed to the effect of internal stresses in the samples due to degradation in HBSS [49].

4. Wear and corrosion modeling of ultrafine mg/ceo$_2$ nanocomposites

A machine learning approach has been developed that utilizes a feedforward neural network and a Long Short-Term Memory (LSTM) network to predict wear and corrosion behavior, respectively, in ultrafine Mg/CeO_2 nanocomposites. The feedforward network is designed to predict wear behavior, and the LSTM network is specially established to describe corrosion behavior by capturing the temporal and sequential

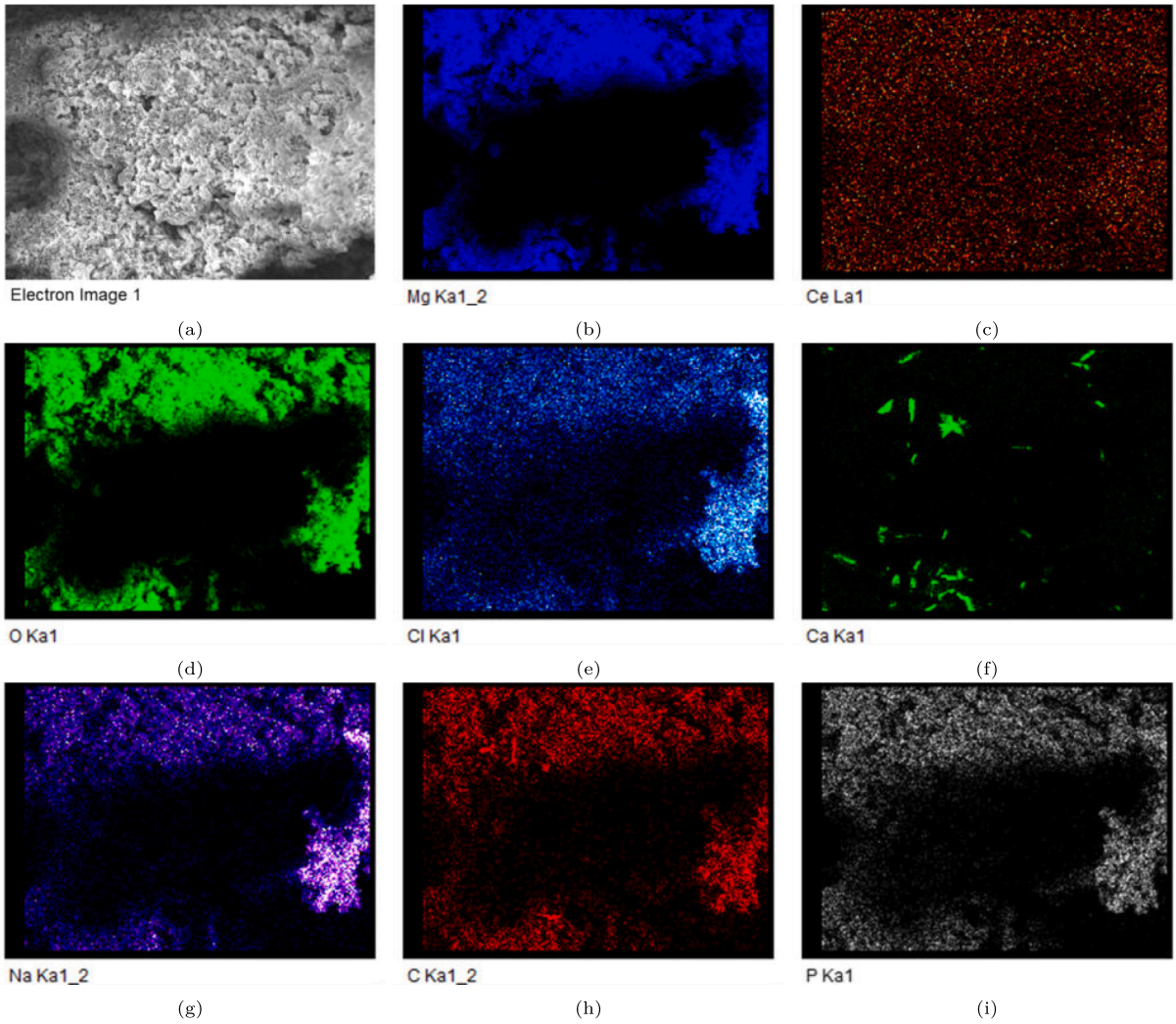

Fig. 20. EDX mapping of Mg/1.0CeO_2 nanocomposite: (a) original picture, (b) Magnesium, (c) Cerium, (d) Oxygen, (e) Chlorine, (f) Calcium, (g) Sodium, (h) Carbon and (i) Phosphorus.

nature of the corrosion process. This approach can offer helpful insights and accurate predictions for the corrosion and wear characteristics of ultrafine Mg/CeO_2 nanocomposites.

4.1. Data preprocessing

The availability of enough training samples considerably impacts the overall performance of machine learning algorithms, including LSTM and feedforward networks [50,51]. An extensive dataset comprising 191,600 corrosion samples and 320,000 wear samples was utilized in this work by employing an appropriate data augmentation approach. To ensure robust training and evaluation, the dataset was partitioned into training, validation, and test subsets using a 70%-15%–15% ratio, respectively. Prior to this, data shuffling was applied, a critical step that ensured that the training, test, and validation sets accurately represented the overall data distribution and achieved improved generalization levels. Additionally, shuffling the training datasets not only enhances testing accuracy but also promotes a more efficient learning process by facilitating better convergence rates [52]. The neural networks underwent training using the training set of the data, and their performance was assessed using the validation set. Subsequently, they were tested on independent datasets to evaluate their ability to make predictions on previously unseen data.

The applied load directly influences the wear processes, accurately reflecting the load-dependent aspects of wear behavior. Similarly, CeO_2 nanoparticles' volume fraction influences the material's wear resistance by affecting its strength and hardness. Therefore, the most important independent factors that may be used as the network input to describe the wear behavior of ultrafine Mg/CeO_2 nanocomposites are applied load and the volume fraction of CeO_2 nanoparticles. Precise assessments of wear rates, mechanisms, and overall wear resistance are made possible by incorporating these variables into machine learning models. In the context of corrosion modeling, the factors that impact the process are immersion time and the volume fraction of CeO_2 nanoparticle. Immersion time provides information on the duration of exposure to corrosive media, which is necessary to effectively capture the time-dependent nature of corrosion processes and predict corrosion rates over certain time periods. The volume fraction, on the other hand, has a direct effect on the nanocomposite's overall corrosion resistance since it turns out to be a measure of the concentration and distribution of CeO_2 nanoparticles throughout the Mg matrix. With the aid of these features, machine learning models can comprehend the complex relationships between exposure duration, volume fraction, and corrosion behavior, providing accurate predictions that contribute to material design, optimization, and the identification of relevant corrosion resistance factors.

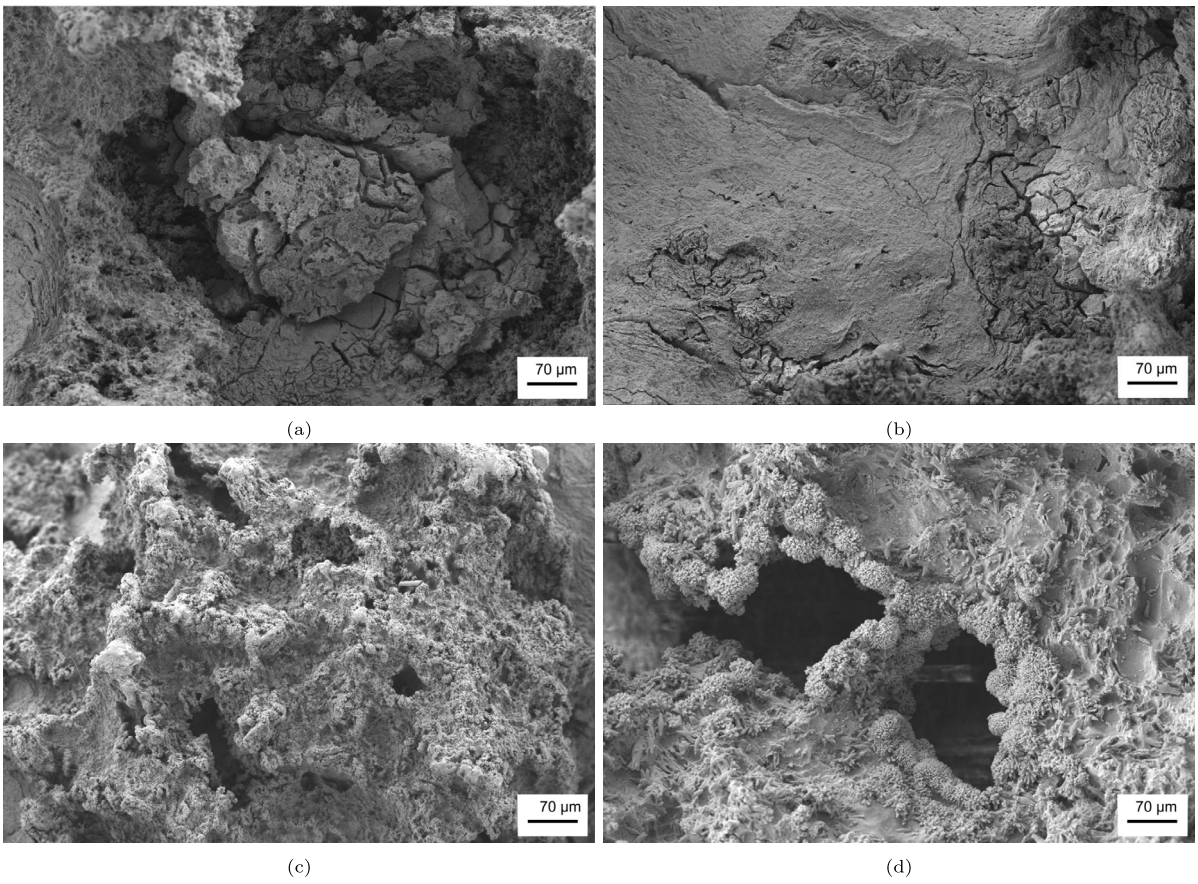

Fig. 21. FESEM micrographs of (a) pure Mg, (b) Mg/0.5CeO_2, (c) Mg/1.0CeO_2 and (d) Mg/1.5CeO_2 nanocomposite after cleaning of corrosion product (post 20 days).

A data augmentation technique is used as a cost-effective alternative to conducting time-consuming and resource-intensive experiments to avoid the challenges raised by an insufficient number of data samples. Working with a limited number of data samples increases the risk of overfitting, even when high R-squared values are achieved, potentially causing the model to capture noise instead of underlying trends [53]. Furthermore, incomplete datasets may not accurately represent the data distribution, which can limit the model's capacity to capture genuine relationships between variables [54]. In the specific context of corrosion and wear rate predictions, networks trained with limited-sized datasets often face challenges in accurately capturing trends for unseen datasets. This signifies the importance of augmenting the data to enhance the practical applicability of predictive models. In doing so, a predictive modeling-based imputation technique with multiple regression analysis is used as a powerful approach for expanding the size of a dataset by creating new samples from the existing data. The technique involves creating a regression model using variables that affect the processes. Multiple regression analysis can capture the connections between these variables to provide precise predictions for missing data. This imputation approach is particularly helpful for wear and corrosion studies since several variables tend to impact these phenomena, and multiple regression may be employed to account for the complex dependencies and interactions among these parameters. For example, the applied force and nanoparticle volume fraction play pivotal roles in determining material wear characteristics. Similarly, during corrosion analysis, factors such as immersion time and nanoparticle volume fraction exert significant influence on the corrosion rate. Missing data on any of these variables can be imputed using their correlations with the other observed variables by incorporating these variables as predictors in the regression model. Moreover, predictive modeling-based imputation using multiple regression helps to reduce bias and improve the quality of subsequent analysis. Therefore, imputing missing data in the context of wear and corrosion analysis leads to more robust statistical analyses and more accurate wear and corrosion behavior predictions.

The core of the predictive modeling-based imputation technique involves employing multiple regression to estimate and impute missing values as follows:

$$Y = \beta_0 + \beta_1 X_1 + \beta_2 X_2 + \ldots + \beta_p X_p + \epsilon \tag{10}$$

where $X_1, X_2, \ldots, X_p$ represent the independent predictor variables and Y the dependent variable with values that are missing. The residual term, ϵ, accounts for the potential unforeseen variation in Y that is not taken into account by the independent variables. It consists of all the variables associated with Y that are not accounted for in the model. A least-squares approach that minimizes the sum of the squared differences between the actual values of Y and the values predicted by the model used to determine the coefficients $\beta_0, \beta_1, \beta_2, \ldots, \beta_p$. The coefficients can be estimated as follows: $\hat{\beta}$:

$$\hat{\beta} = (X^\top X)^{-1} X^\top Y \tag{11}$$

where Y is the dependent variable's vector and X is the predictor variables' matrix.

The next crucial step in data preparation for predicting wear and corrosion rates involves the normalization of input features. This transformation ensures that variables are on a uniform scale and eliminates the influence of differing units. To achieve this, Z-score normalization, also known as standardization, is employed, which scales the data to have a mean of zero and a standard deviation of one. Specifically, for wear modeling, the input features of applied load and particle volume fraction are normalized, while for corrosion modeling, immersion time

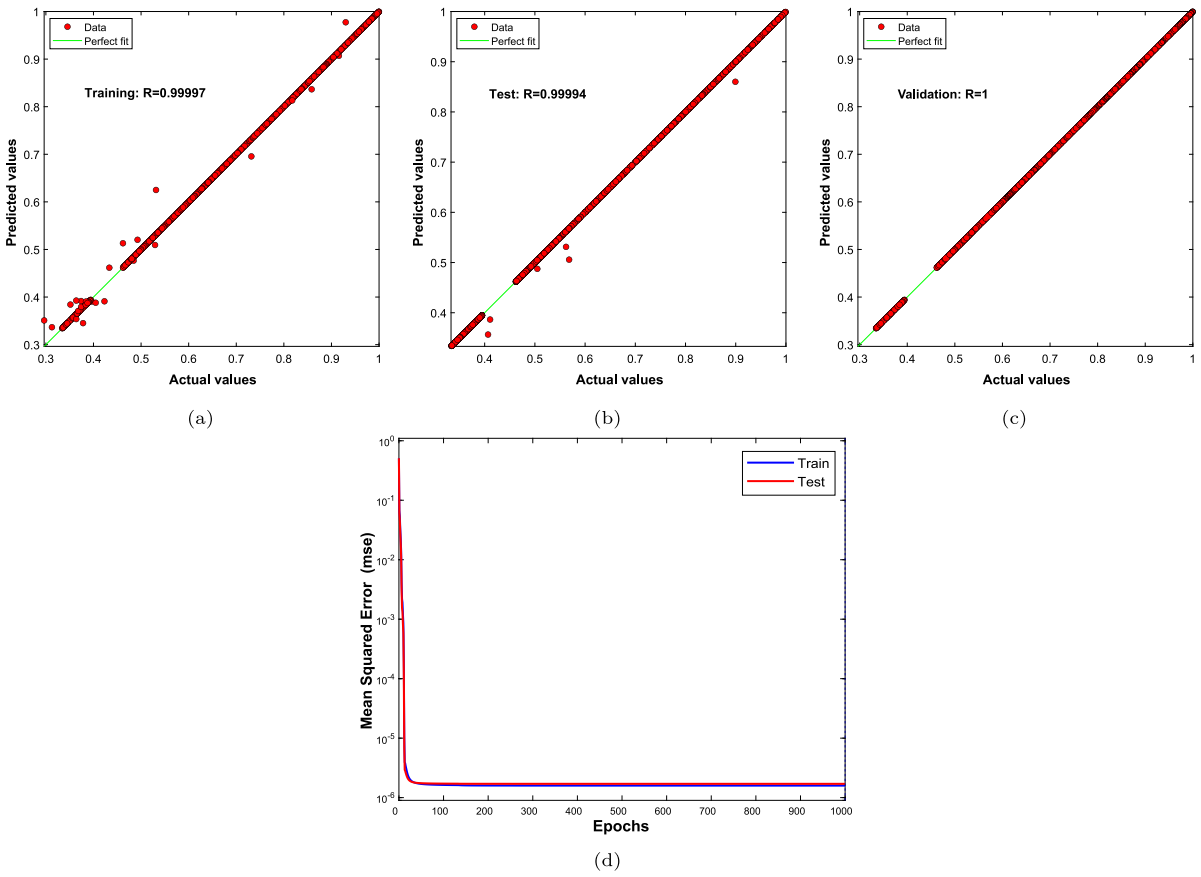

Fig. 22. (a–c) the regression analysis conducted using the feedforward network to predict the wear rates of ultrafine Mg/CeO_2 nanocomposites. (d) the Mean Square Error (MSE) versus the number of epochs for both the test and training datasets. Notably, the best training performance, reaching a value of 1.59e−06, is achieved at epoch 1000.

and particle volume fraction are normalized. The normalized value for each data point x can be obtained by

$$z = \frac{x - \mu}{\sigma} \tag{12}$$

where the mean and standard deviation of the dataset are denoted by μ and σ, respectively. It is important to note that denormalizing the predicted wear and corrosion rates is necessary once the neural network model predicts the outputs—this is necessary to obtain meaningful and understandable results. The Z-score denormalization process can be done by reversing the normalization process using the original data's mean and standard deviation.

4.2. Wear rate prediction with feedforward neural networks

Feedforward neural networks, also known as multilayer perceptrons (MLPs), exhibit the ability for applications without sequential or temporal relationships in the data, such as the wear process [55,56]. Feedforward neural networks can handle big datasets and model nonlinear interactions by virtue of their layered architecture and activation functions. They have shown to be a useful tool for assessing key input variables and extracting meaningful patterns that facilitate predicting wear rates in the context of wear analysis [57].

The experimental dataset encompasses wear rates observed in the nanocomposite, considering volume fractions of 0.5%, 1%, and 1.5%, and varying applied loads of 5 N, 9 N, and 13 N. In this configuration, the input features comprise volume fraction and applied loads, while the target values employed for training the feedforward network are the wear rates. The proposed feedforward network architecture includes an input layer with two units specifically designed to process normalized applied load and volume fraction. It incorporates two hidden layers, each consisting of 10 perceptrons utilizing the hyperbolic tangent sigmoid transfer function. This choice of transfer function offers advantages such as non-linearity and smooth activation. The output layer, composed of a single cell, employs a linear transfer function to generate predictions for normalized wear rates. To enhance generalization and mitigate overfitting, the network is trained using the Bayesian regularization back-propagation algorithm. This algorithm effectively strikes a balance between model complexity and data fitting, ensuring the robustness of the configuration for accurately predicting wear rates in ultrafine Mg/CeO_2.

Figs. 22a–c illustrate the regression analysis performed on training, test, and validation datasets. It turns out that the network has established the correlation between the predicted and target values, as evidenced by the r values approaching 1 in all cases. The coefficient of determination was determined for each regression analysis to evaluate the goodness of the fitting process. Fig. 22d shows the performance of the proposed network in terms of the Mean Square Error (MSE) metric. The MSE was continuously reduced as the number of epochs grew, which indicated that the results were converging. The best training performance, with an MSE of 1.59e−06, was achieved at epoch 1000.

Fig. 23 shows that the proposed feedforward network can accurately predict the wear rate of ultrafine Mg/CeO_2 based on the input features of the applied load and volume fraction of CeO_2 nanoparticles. The Network has learned about complex relationships between these features and their resulting wear rates by training on a comprehensive dataset. In particular, the network's prediction results conform closely to experimental observations and thus give confidence in its ability to predict. The network's prediction results also show a trend whereby an increase in volume fraction leads to a decrease in the wear rate. This observation is consistent with experiments, further confirming

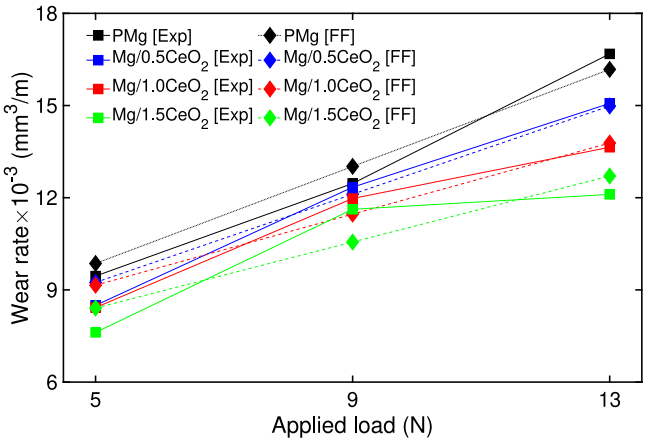

Fig. 23. Comparison of predicted and experimental wear rates versus applied load for ultrafine Mg/CeO_2 nanocomposites with various volume fractions.

the Network's ability to gain insight into the core physics of ultrafine Mg/CeO_2 wear.

4.3. Corrosion rate prediction with LSTM networks

This section explores the use of Long Short-Term Memory (LSTM) networks, which are a subtype of recurrent neural networks, to predict corrosion rates. LSTM networks are a powerful deep-learning model for capturing complex sequential and temporal relationships due to their outstanding features in tackling time-related features [58,59]. Corrosion is a prominent example of such processes in which time plays a crucial role. It is now feasible to capture long-term dependencies and handle different durations of time-related data by utilizing the memory cells and gating mechanisms inside LSTM networks.

The experimental dataset includes corrosion rates of the nanocomposite with volume fractions of 0.5%, 1%, and 1.5% at various immersion times of 24 h, 96 h, 144 h, 168 h, 192 h, 312 h, 384 h, and 480 h. In this setup, volume fraction and immersion times serve as input features, while corrosion rates act as the target values to train the LSTM networks. The proposed network architecture for predicting corrosion rates comprises an input layer with two units designed specifically to process normalized immersion time and volume fraction. The architecture also incorporates a two-hidden-layer configuration, with each hidden layer consisting of 12 units. The initial hidden layer is responsible for processing input features, extracting essential temporal dependencies, and initiating the representation-building process. Subsequently, the second hidden layer enhances these representations by capturing intricate temporal patterns. The output layer, composed of a single unit, generates normalized corrosion rate predictions based on the processed data. The LSTM cells, which incorporate memory cells and gating mechanisms, optimize learning rates through the dynamic adaptation provided by the Adam algorithm, adjusting based on gradient moments. This adaptive approach ensures accurate predictions while effectively handling time-related data of varying lengths.

Fig. 24a–c shows the results of the regression analysis performed on training, test, and validation datasets. For each investigation, the coefficient of determination was determined to measure how well the network performed the fitting process. It is noteworthy that $r = 1$ indicates a perfect match that encompasses all data variability. It turns out that the network has been effectively trained and developed a significant correlation between the predicted and target values because the r values for all cases are extremely close to 1. Further evaluation is shown in Fig. 24d, which points out the performance of the developed network in terms of the Mean Square Error (MSE) metric. As the number of epochs increases, the MSE consistently decreases, indicating that the network's predictions gradually align more closely with the actual values during training. Notably, at epoch 100, the network achieves optimal training performance, with an MSE of 1.10e−03. In this context, an epoch refers to a complete iteration where the entire dataset passes through the network, contributing to its learning and refinement.

Fig. 25 points out that using the input features of the immersion time and the volume fraction of CeO_2 nanoparticles, the developed LSTM network can effectively predict and model the corrosion rate of ultrafine Mg/CeO_2. The underlying patterns and relationships between those features are taught to the network by training in a dataset containing these features and corresponding corrosion rates. The Network's predictions are consistent with the actual rate of corrosion, demonstrating its efficient modeling ability. Furthermore, the LSTM network reveals an important trend in the relationship between volume fraction and corrosion rate. The network demonstrates that the corrosion rate decreases as the volume fraction increases. This finding is in line with experimental observations, where higher volume fractions of certain nanocomposites have been shown to exhibit reduced corrosion rates. The ability of the LSTM network to capture and replicate this relationship further validates its effectiveness in understanding and predicting the behavior of nanocomposites.

5. Conclusion

This paper has investigated rare earth oxide-mediated ultrafine Mg nanocomposites' microstructural, tribological, and corrosion properties. The Mg/CeO_2 nanocomposites were synthesized by high energy ball milling assisted in-situ hot extrusion-based powder metallurgy process. The following is a brief summary of the findings:

1. An increase in the vol.% of CNPs increased the microhardness of Mg/CeO_2 nanocomposites. In comparison to the unreinforced Mg, the average value of the microhardness improved by 17.58%, 30.37%, and 68.09% for $Mg/0.5CeO_2$, $Mg/1.0CeO_2$ and $Mg/1.5CeO_2$ respectively. Moreover, near-uniform microhardness values can be seen for pure Mg, $Mg/0.5CeO_2$ and $Mg/1.0CeO_2$ nanocomposite samples. However, at higher vol.% of CNPs (1.5 vol.%), a non-homogeneous distribution of the microhardness can be seen. This could be due to the agglomeration of nanoparticles at higher volume fractions.
2. The wear rate of nanocomposites increased with the increase in applied load and decreased with the increase in vol.% of reinforcement. $Mg/1.5CeO_2$ had the lowest wear rate, which was 0.207 mm^3/m at a 13 N load. It was 11.64% lower than pure Mg. Abrasion, delamination, ploughing, and oxidation are the most prevalent mechanisms acknowledged on the worn surfaces of all the samples.
3. The value of the friction coefficient of nanocomposites improved with the increase in applied load and reinforcement content. This is because CNPs carried a significant portion of the load and reduced the importance of adhesive wear. Moreover, higher loads reduced abrasive wear damage and increased oxidation, thereby lowering the COF values.
4. Compared to pure Mg, the corrosion rates of the nanocomposites containing 0.5, 1.0, and 1.5 vol.% CNPs were reduced by 43%, 42%, and 70%, respectively, in HBSS at 37 °C. Moreover, EDX analysis identified a Ca:P ratio of 1:1.87 for the nanocomposites, which is close to the Ca:P ratio required for bone mineralization. Therefore, Mg/CeO_2 nanocomposites showed considerable promise for use as bioresorbable temporary implants.

Furthermore, two neural networks have been developed to predict nanocomposites' wear and corrosion behavior. The first model employs a feedforward network to estimate wear rates using the applied load

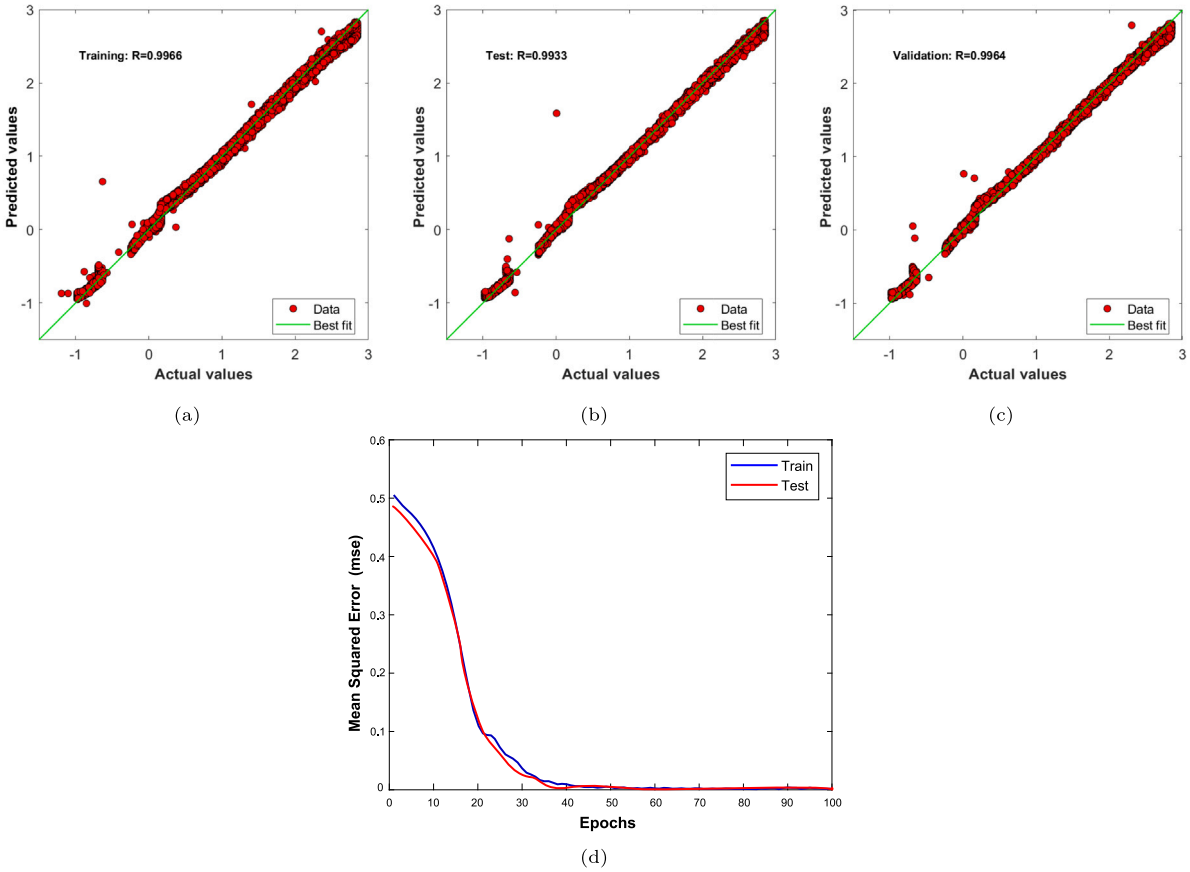

Fig. 24. (a–c) the regression analysis conducted using the LSTM network to predict the corrosion rates of ultrafine Mg/CeO_2 nanocomposites. (d) the Mean Square Error (MSE) versus the number of epochs for both the test and training datasets. Notably, the best training performance, reaching a value of 1.10e−03, is achieved at epoch 100.

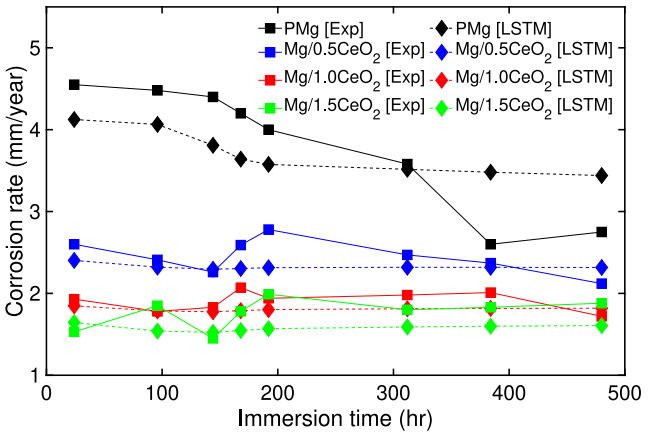

Fig. 25. Comparison of predicted and experimental corrosion rates versus immersion time for ultrafine Mg/CeO_2 nanocomposites with various volume fractions.

and volume fraction as the input parameters. The second model is an LSTM network that anticipates corrosion rates using the immersion time and volume fraction as inputs. The effectiveness of these models in predicting nanocomposites' wear and corrosion performance has been examined by comparing the network prediction results with experimental test results. This comparison reveals that these models' predicted results closely match the data obtained from wear and corrosion experiments. The predictive capabilities of these models provide valuable insights for understanding and optimizing the performance of nanocomposite materials in wear and corrosion-related applications.

Declaration of competing interest

The authors declare that they have no known competing financial interests or personal relationships that could have appeared to influence the work reported in this paper.

Data availability

Data will be made available on request.

Acknowledgments

S.D. and A.M. sincerely acknowledge the financial support from the ASEAN-Indian Science and Technology Development Fund (AISTDF), DST, Govt. of India, under Grant No. IMRC/AISTDF/R&D/P-14/2018. F.M. acknowledges the partial support provided by the AGÜ foundation.

The authors appreciate DST, India, for providing a 3D profilometer characterization facility through the FIST project grant number SR/FST/ET-II/2018/222(C).

References

[1] Munir K, Wen C, Li Y. Graphene nanoplatelets-reinforced magnesium metal matrix nanocomposites with superior mechanical and corrosion performance for biomedical applications. J Magnes Alloy 2020;8(1):269–90.

[2] Shahin M, Munir K, Wen C, Li Y. Magnesium matrix nanocomposites for orthopedic applications: a review from mechanical, corrosion, and biological perspectives. Acta Biomater 2019;96:1–19.

[3] Shahin M, Wen C, Munir K, Li Y. Mechanical and corrosion properties of graphene nanoplatelet–reinforced Mg–Zr and Mg–Zr–Zn matrix nanocomposites for biomedical applications. J Magnes Alloy 2022;10(2):458–77.

[4] Hiromoto S, Shishido T, Yamamoto A, Maruyama N, Somekawa H, Mukai T. Precipitation control of calcium phosphate on pure magnesium by anodization. Corros Sci 2008;50(10):2906–13.

[5] Bairagi D, Mandal S. A comprehensive review on biocompatible mg-based alloys as temporary orthopaedic implants: Current status, challenges, and future prospects. J Magnes Alloy 2022;10(3):627–69.

[6] Shahin M, Munir K, Wen M, Wen C, Li Y. Microstructure, mechanical and corrosion properties of hot-pressed graphene nanoplatelets-reinforced mg matrix nanocomposites for biomedical applications. J Alloys Compd 2021;887:161379.

[7] Tekumalla S, Nandigam Y, Bibhanshu N, Rajashekara S, Yang C, Suwas S, et al. A strong and deformable in-situ magnesium nanocomposite igniting above 1000 C. Sci Rep 2018;8(1):7038.

[8] Khalili MA, Tamjid E. Controlled biodegradation of magnesium alloy in physiological environment by metal organic framework nanocomposite coatings. Sci Rep 2021;11(1):8645.

[9] Parande G, Manakari V, Gupta H, Gupta M. Magnesium-β-tricalcium phosphate composites as a potential orthopedic implant: A mechanical/damping/immersion perspective. Metals 2018;8(5):343.

[10] Guo Y, Wang S, Liu W, Sun Z, Zhu G, Xiao T. Effect of laser shock peening on tribological properties of magnesium alloy zk60. Tribol Int 2020;144:106138.

[11] Kaviti RVP, Jeyasimman D, Parande G, Gupta M, Narayanasamy R. Investigation on dry sliding wear behavior of Mg/Bn nanocomposites. J Magnes Alloy 2018;6(3):263–76.

[12] Kumar KA, Pillai U, Pai B, Chakraborty M. Dry sliding wear behaviour of Mg–Si alloys. Wear 2013;303(1–2):56–64.

[13] Yang Z, Wang S, Zhao Y, Wei M. Evaluation of wear characteristics of Al3tip/Mg composite. Mater Charact 2010;61(5):554–63.

[14] Nguyen Q, Sim Y, Gupta M, Lim C. Tribology characteristics of magnesium alloy az31b and its composites. Tribol Int 2015;82:464–71.

[15] Rahmani K, Sadooghi A, Hashemi S. The effect of Al2O3 content on tribology and corrosion properties of Mg-Al2O3 nanocomposites produced by single and double-action press. Mater Chem Phys 2020;250:123058.

[16] Gnanavelbabu A, Vinothkumar E, Ross NS, Gupta MK, Jamil M. Tribo-corrosive wear and mechanical properties of nanoparticles reinforced Mg-az91d composites. Tribol Int 2023;178:108054.

[17] Turan ME, Sun Y, Akgul Y, Turen Y, Ahlatci H. The effect of GNPs on wear and corrosion behaviors of pure magnesium. J Alloys Compd 2017;724:14–23.

[18] Razavi M, Fathi M, Meratian M. Fabrication and characterization of magnesium–fluorapatite nanocomposite for biomedical applications. Mater Charact 2010;61(12):1363–70.

[19] Montemor M, Pinto R, Ferreira M. Chemical composition and corrosion protection of silane films modified with CeO2 nanoparticles. Electrochim Acta 2009;54(22):5179–89.

[20] Eduok U, Faye O, Tiamiyu A, Szpunar J. Fabricating protective epoxy-silica/CeO2 films for steel: Correlating physical barrier properties with material content. Mater Des 2017;124:58–68.

[21] Li J, Wen J, Li B, Li W, Qiao W, Shen J, et al. Valence state manipulation of cerium oxide nanoparticles on a titanium surface for modulating cell fate and bone formation. Adv Sci 2018;5(2):1700678.

[22] Montemor M, Ferreira M. Analytical characterization of silane films modified with cerium activated nanoparticles and its relation with the corrosion protection of galvanised steel substrates. Prog Org Coat 2008;63(3):330–7.

[23] Kujur MS, Manakari V, Parande G, Tun KS, Mallick A, Gupta M. Enhancement of thermal, mechanical, ignition and damping response of magnesium using nano-ceria particles. Ceram Int 2018;44(13):15035–43.

[24] Kujur MS, Manakari V, Parande G, Prasadh S, Wong R, Mallick A, et al. Development of rare-earth oxide reinforced magnesium nanocomposites for orthopaedic applications: A mechanical/immersion/biocompatibility perspective. J Mech Behav Biomed Mater 2021;114:104162.

[25] Rahmani K, Sadooghi A, Nokhberoosta M. The effect of the double-action pressure on the physical, mechanical and tribology properties of Mg-wo3 nanocomposites. J Mater Res Technol 2020;9(1):1104–18.

[26] Penther D, Ghasemi A, Riedel R, Fleck C, Kamrani S. Effect of SiC nanoparticles on manufacturing process, microstructure and hardness of Mg-Sic nanocomposites produced by mechanical milling and hot extrusion. Mater Sci Eng A 2018;738:264–72.

[27] Casati R, Vedani M. Metal matrix composites reinforced by nano-particles—A review. Metals 2014;4(1):65–83.

[28] Hasan MS, Kordijazi A, Rohatgi PK, Nosonovsky M. Triboinformatic modeling of dry friction and wear of aluminum base alloys using machine learning algorithms. Tribol Int 2021;161:107065.

[29] Lanzoni D, Rovaris F, Montalenti F. Machine learning potential for interacting dislocations in the presence of free surfaces. Sci Rep 2022;12(1):3760.

[30] Aydin F, Durgut R, Mustu M, Demir B. Prediction of wear performance of Zk60/CeO2 composites using machine learning models. Tribol Int 2023;177:107945.

[31] Kavimani V, Prakash KS, Thankachan T. Experimental investigations on wear and friction behaviour of SiC@ r-GO reinforced mg matrix composites produced through solvent-based powder metallurgy. Composites B 2019;162:508–21.

[32] Pagadala ND, Radha R, et al. Machine learning based corrosion prediction of as cast mg-sn alloys for biomedical applications. Mater Today Commun 2023;35:106108.

[33] Chaluvaraju B, Afzal A, Vinnik DA, Kaladgi AR, Alamri S, Tirth V. Mechanical and corrosion studies of friction stir welded nano al2o3 reinforced al-mg matrix composites: Rsm-ann modelling approach. Symmetry 2021;13(4):537.

[34] Saheb N. Characterization of mechanically milled and spark plasma sintered al2124-cnt nanocomposites. Sci Sinter 47(2).

[35] Akbaripanah F, Sabbaghian M, Fakhar N, Minárik P, Veselỳ J, Hung P, et al. Influence of high pressure torsion on microstructure evolution and mechanical properties of az80/SiC magnesium matrix composites. Mater Sci Eng A 2021;826:141916.

[36] Zahmatkesh B, Enayati M. A novel approach for development of surface nanocomposite by friction stir processing. Mater Sci Eng A 2010;527(24–25):6734–40.

[37] Asadi P, Faraji G, Masoumi A, Besharati Givi M. Experimental investigation of magnesium-base nanocomposite produced by friction stir processing: effects of particle types and number of friction stir processing passes. Metall Mater Trans A 2011;42:2820–32.

[38] Arab M, Marashi S. Graphene nanoplatelet (GNP)-incorporated az31 magnesium nanocomposite: microstructural, mechanical and tribological properties. Tribol Lett 2018;66:1–11.

[39] Fida Hassan S, Al-Qutub A, Tun K, Gupta M. Study of wear mechanisms of a novel magnesium based hybrid nanocomposite. J Tribol 2015;137(1):011601.

[40] Monikandan V, Joseph M, Rajendrakumar P, Sreejith M. Tribological behavior of liquid metallurgy-processed aa 6061-b4c composites. Mater Res Express 2015;2(1):016507.

[41] Kai X, Li Z, Fan G, Guo Q, Xiong D, Zhang W, et al. Enhanced strength and ductility in particulate-reinforced aluminum matrix composites fabricated by flake powder metallurgy. Mater Sci Eng A 2013;587:46–53.

[42] Suh NP. The delamination theory of wear. Wear 1973;25(1):111–24.

[43] Beck Jr GR, Ha S-W, Camalier CE, Yamaguchi M, Li Y, Lee J-K, et al. Bioactive silica-based nanoparticles stimulate bone-forming osteoblasts, suppress bone-resorbing osteoclasts, and enhance bone mineral density in vivo. Nanomed Nanotechnol Biol Med 2012;8(6):793–803.

[44] Sahoo S. Recent advances in layered materials and structures. Springer; 2021.

[45] Pu Z, Song G-L, Yang S, Outeiro J, Dillon Jr O, Puleo D, et al. Grain refined and basal textured surface produced by burnishing for improved corrosion performance of az31b Mg alloy. Corros Sci 2012;57:192–201.

[46] Okada M, Matsumoto T. Synthesis and modification of apatite nanoparticles for use in dental and medical applications. Jpn Dent Sci Rev 2015;51(4):85–95.

[47] Ratna Sunil B, Sampath Kumar T, Chakkingal U, Nandakumar V, Doble M. Nano-hydroxyapatite reinforced az31 magnesium alloy by friction stir processing: a solid state processing for biodegradable metal matrix composites. J Mater Sci, Mater Med 2014;25:975–88.

[48] Parande G, Manakari V, Prasadh S, Chauhan D, Rahate S, Wong R, et al. Strength retention, corrosion control and biocompatibility of Mg–Zn–Si/Ha nanocomposites. J Mech Behav Biomed Mater 2020;103:103584.

[49] Vojtěch D, Kubásek J, Šerák J, Novák P. Mechanical and corrosion properties of newly developed biodegradable Zn-based alloys for bone fixation. Acta Biomater 2011;7(9):3515–22.

[50] Singh V, Pencina M, Einstein AJ, Liang JX, Berman DS, Slomka P. Impact of train/test sample regimen on performance estimate stability of machine learning in cardiovascular imaging. Sci Rep 2021;11(1):14490.

[51] Ng W, Minasny B, Mendes WdS, Demattê JAM. The influence of training sample size on the accuracy of deep learning models for the prediction of soil properties with near-infrared spectroscopy data. Soil 2020;6(2):565–78.

[52] Mao G, Wang M, Liu J, Wang Z, Wang K, Meng Y, et al. Comprehensive comparison of artificial neural networks and long short-term memory networks for rainfall-runoff simulation. Phys Chem Earth A/B/C 2021;123:103026.

[53] Jabbar H, Khan RZ. Methods to avoid over-fitting and under-fitting in supervised machine learning (comparative study). Comput Sci Commun Instrum Devices 2015;70(10.3850):978–81.

[54] Althnian A, AlSaeed D, Al-Baity H, Samha A, Dris AB, Alzakari N, et al. Impact of dataset size on classification performance: an empirical evaluation in the medical domain. Appl Sci 2021;11(2):796.

[55] Cinar AC. Training feed-forward multi-layer perceptron artificial neural networks with a tree-seed algorithm. Arab J Sci Eng 2020;45(12):10915–38.

[56] Dinaharan I, Palanivel R, Murugan N, Laubscher R. Application of artificial neural network in predicting the wear rate of copper surface composites produced using friction stir processing. Aust J Mech Eng 2022;20(4):1079–90.

[57] Paturi UMR, Cheruku S, Reddy N. The role of artificial neural networks in prediction of mechanical and tribological properties of composites—a comprehensive review. Arch Comput Methods Eng 2022;29(5):3109–49.

[58] Lindemann B, Müller T, Vietz H, Jazdi N, Weyrich M. A survey on long short-term memory networks for time series prediction. Proc CIRP 2021;99:650–5.

[59] Sutskever I, Vinyals O, Le QV. Sequence to sequence learning with neural networks. Adv Neural Inf Process Syst 2014;27.